Signal Processing Systems
Mekelweg 4,
2628 CD Delft
The Netherlands
https://sps.ewi.tudelft.nl/

SPS-2024-00

M.Sc. Thesis

Sparse Non-uniform Optical Phased Array Design

Kunlei Yu B.Eng.

Abstract

This thesis addresses the design and optimization of sparse non-uniform optical phased arrays (OPAs) for advanced automotive LiDAR systems. As autonomous driving technologies advance, the demand for high-resolution, reliable, and compact LiDAR systems has become increasingly critical. Traditional uniform OPAs, while effective, face limitations regarding power consumption. This work introduces an innovative approach to designing sparse non-uniform OPAs that achieve desired performance metrics essential for automotive applications, including beamwidth, field of view, and sidelobe levels, while minimizing element count and, consequently, energy consumption.

Through mathematical modelling and simulation, we formulate the problem of sparse OPA design as an optimization problem, leveraging techniques from compressive sensing to identify the most efficient element arrangements. We propose using the sparse array synthesis method to formulate the sparse OPA design problem, utilizing algorithms such as LASSO, thresholding, and iterative reweighted l1-norm minimization to achieve optimal sparse configurations. Our results demonstrate substantial improvements in effectiveness, offering a practical solution to the constraints posed by current LiDAR systems. This thesis contributes to the field by providing a comprehensive framework for the design of sparse non-uniform OPAs, highlighting the trade-offs and benefits of various design strategies. The findings advance our understanding of OPA design principles.

Sparse Non-uniform Optical Phased Array Design

Thesis

submitted in partial fulfillment of the
requirements for the degree of

Master of Science

in

Electrical Engineering

by

Kunlei Yu B.Eng.
born in Luoyang, China

This work was performed in:

Signal Processing Systems Group
Department of Microelectronics
Faculty of Electrical Engineering, Mathematics and Computer Science
Delft University of Technology

Delft University of Technology

Delft University of Technology
Department of
Microelectronics

The undersigned hereby certify that they have read and recommend to the Faculty of Electrical Engineering, Mathematics and Computer Science for acceptance a thesis entitled **"Sparse Non-uniform Optical Phased Array Design"** by **Kunlei Yu B.Eng.** in partial fulfillment of the requirements for the degree of **Master of Science**.

Dated: 21 March 2024

Chairman: _____
prof.dr.ir. G.J.T. Leus

Advisors: _____
dr. Geethu Joseph

_____
dr.ir. Jac Romme

Committee Members: _____
dr.ir. J.N. Driessen

_____

Abstract

This thesis addresses the design and optimization of sparse non-uniform optical phased arrays (OPAs) for advanced automotive LiDAR systems. As autonomous driving technologies advance, the demand for high-resolution, reliable, and compact LiDAR systems has become increasingly critical. Traditional uniform OPAs, while effective, face limitations regarding power consumption. This work introduces an innovative approach to designing sparse non-uniform OPAs that achieve desired performance metrics essential for automotive applications, including beamwidth, field of view, and sidelobe levels, while minimizing element count and, consequently, energy consumption.

Through mathematical modelling and simulation, we formulate the problem of sparse OPA design as an optimization problem, leveraging techniques from compressive sensing to identify the most efficient element arrangements. We propose using the sparse array synthesis method to formulate the sparse OPA design problem, utilizing algorithms such as LASSO, thresholding, and iterative reweighted l1-norm minimization to achieve optimal sparse configurations. Our results demonstrate substantial improvements in effectiveness, offering a practical solution to the constraints posed by current LiDAR systems. This thesis contributes to the field by providing a comprehensive framework for the design of sparse non-uniform OPAs, highlighting the trade-offs and benefits of various design strategies. The findings advance our understanding of OPA design principles.

Acknowledgments

My master's journey at Delft University of Technology has come to an end. Along this journey, I have harvested a deeper understanding about the world of engineering, as well as enlightenment and joy. I am deeply grateful for my commitment and curiosity, which have guided and motivated me to this pivotal juncture. Naturally, I did not traverse this path alone; the assistance of numerous individuals has been invaluable to me. Thus, I wish to extend my sincerest gratitude to them here.

First and foremost, I wish to express my deepest appreciation to my supervisors, dr. Geethu Joseph and dr.ir. Jac Romme. They guided me into the world of research, investing substantial time and energy. I am very grateful for the considerable freedom I enjoyed, making my journey both fun and informative. Their unique perspectives and profound insights continually provoked fresh inspirations, propelling me towards refinement and advancement in my research. Additionally, I would like to extend special thanks to my advisor, prof.dr.ir. G.J.T. Leus , for introducing me to this intriguing and challenging project, as well as all the lectures he delivered. Furthermore, I would like to extend my appreciation to dr.ir. J.N. Driessen for accepting the invitation to join my thesis committee.

My academic journey was not alone; I walked alongside many esteemed companions. I am grateful to the people in the SPS group and fellow students with whom I learned and explored world of knowledge. Special thanks to the fellow students with whom I had chats in the office on the 18th floor of EWI. Additionally, I wish to extend a special acknowledgment to Yanbin He, whose scholarly insights and encouragement enriched my thesis profoundly. I earnestly wish him a triumph in his career.

Lastly, I extend profound gratitude to my parents for their selfless encouragement in my academic pursuits. Their unwavering dedication has afforded me the liberty to immerse myself in scholarly pursuits without constraint. They have shielded and fortified me with boundless love. Furthermore, I am grateful for a cherished individual I encountered in the Netherlands, Ziqi, with anticipation for the journey ahead together.

As my journey at Delft University of Technology nears its closure, though bittersweet, it signifies the opening of a new chapter in my life. Armed with the knowledge and personal growth cultivated at TU Delft, I am poised to embrace the future with confidence.

Kunlei Yu B.Eng.
Delft, The Netherlands
21 March 2024

Contents

List of Figures

List of Tables

1 Introduction

In recent years, LiDAR (Light detection and ranging) technology has emerged as a cornerstone in the realm of remote sensing and autonomous systems. Especially in automotive applications, LiDAR systems are pivotal in capturing detailed and accurate three-dimensional information about the surroundings. This information is used for advanced driver-assistance systems (ADAS) and autonomous driving vehicles.

A typical LiDAR system emits a pulsed light wave towards a target direction. When the pulse bounces back and is captured by the receiver, the distance to the object in the target direction can be calculated based on the time of flight (ToF). By steering the beam and repeating this measurement process in multiple directions, the system acquires several distance measurements of its surroundings [4]. These distance measurements can then be used to generate a 3D point cloud representation of the environment, as shown in Fig.1.1.

Figure 1.1: An example of 3D map from LiDAR (Source: Velodyne Lidar, Inc.)

LiDAR has demonstrated superior performance over radar in terms of angular resolution and accuracy due to its significantly smaller working wavelength. Additionally, LiDAR excels in providing accurate objective classification through point clouds, offering a detailed representation of the shape and distance of surrounding objects [5]. As an active sensor, LiDAR's robustness to ambient lighting conditions significantly surpasses that of the passive sensor camera, showcasing its advantage in various lighting scenarios [5, 6]. With the increasing demand for more sophisticated LiDAR solutions, researchers and engineers are actively exploring innovative technologies to further enhance the performance, efficiency, and adaptability of these systems.

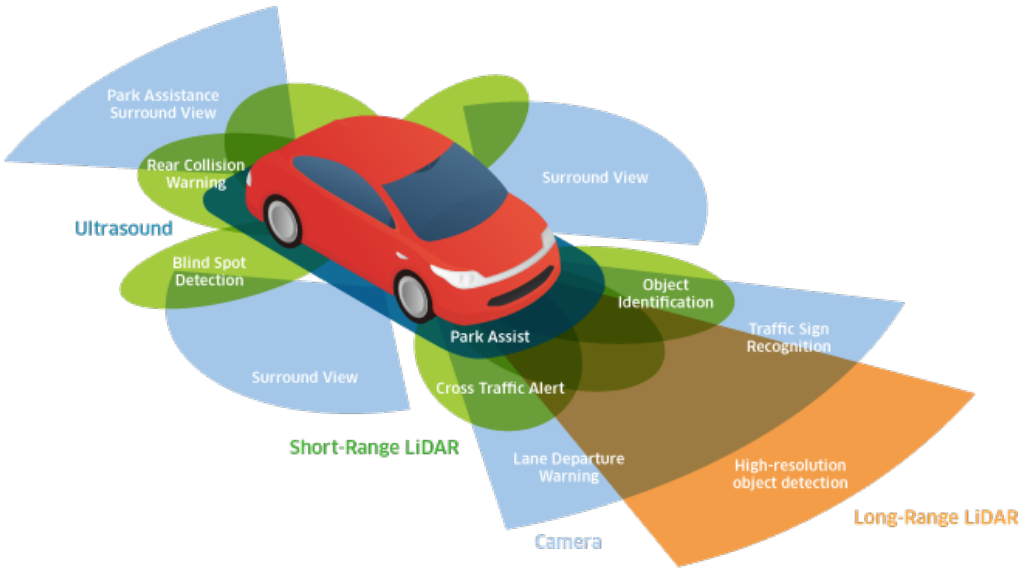

Figure 1.2: A sensor-coverage diagram for ADAS functions (Source: Lumentum Holdings, Inc.)

1.1 Requirements for Automotive Applications

Automotive applications require LiDAR systems for multiple ADAS functions, including functions such as parking assistance and object detection for collision avoidance. A diagram Fig.1.2 demonstrates these functions and corresponding coverage. The requirements depend on the specific ADAS function and the target scenario, including speed, characteristics of objects, the direction of detection (front, side, or rear).

Among the various ADAS functions, collision avoidance requires high-resolution object detection over long distances, up to 200 m, and a specific field of view (FOV) that covers the road ahead, warning the driver if objects appear in the vehicle's trajectory. Higher speeds require longer detection ranges to provide sufficient time for the vehicle to react and stop safely. For instance, detecting potential static obstacles on highways requires a detection range of 200 m to enable emergency braking at high vehicle speeds [1], underscoring the need for high-resolution detection.

As the LiDAR-based detection algorithms perform on the point clouds, Fig.1.3 illustrates the working principle of LiDAR in generating point clouds. Recall that LiDAR generates point clouds by calculating the ToF. Assuming the reflected beam is collimated with the emitting beam, LiDAR detects the blocks (in grey) along the blue arrow in Fig.1.3 by projecting the light on the target block (in black) and calculating the ToF of the reflected light.

The general definition of angular resolution is the minimum angular distance between two objects that can be resolved. According to the working principles of the LiDAR system, the angular resolution refers to the angle of two adjacent scanning

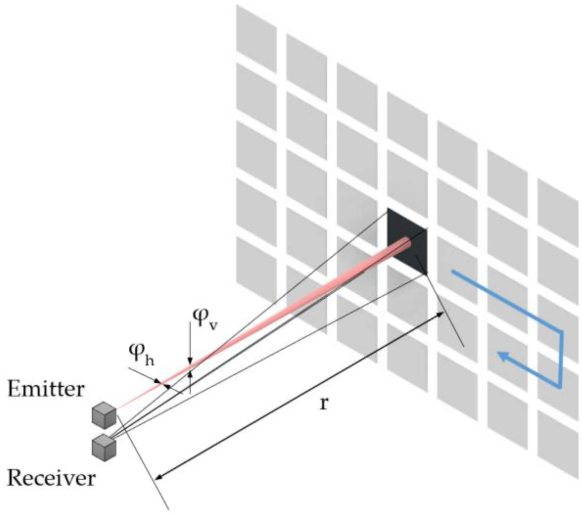

Figure 1.3: The illustration of the working principle of LiDAR system in generating point clouds. The red cone represents the laser beam. The spread area determines the minimum size of the block at a given distance r (ϕ_h is the horizontal beamwidth, ϕ_v is the vertical beamwidth, and r is the distance) [1].

points (centre of a block) [1]. As shown in Fig.1.3, the minimum angle of two adjacent scanning points depends on the size of the beam spread area, which determines the smallest scanning block size. The beam spread area can be measured by beamwidth in angle (ϕ_h and ϕ_v in Fig.1.3). Moreover, the object detection algorithms must be considered in determining the required angular resolution as it directly affects detection performance. Thus, the range of detection, point clouds based algorithms and size of object determine the required angular resolution, equivalent to the width of the laser beam (ϕ_h and ϕ_v).

In this project, we focus on an extreme scenario, driving on a highway, and a specific ADAS function, forward vehicle collision warning, which requires the longest detection range due to the high speed, resulting in the highest angular resolution within a field of view enough to cover the road in front. According to [1], the reasoning for the specific requirements is as follows:

- **Detection Range**: The minimum detection range is 200 m to avoid forward collisions, assuming the subject vehicle is at a speed of 140 km/h. The overtaking manoeuvre requires a warning distance of 180 m, assuming both subject and oncoming vehicles are at 100 km/h on the road without designated overtaking lanes [1].

- **Field of View (FoV)**: The field of view is determined by the range and the width of the road that needs to be covered. It increases when the road in front is not straight. A more curved road requires a larger field of view to cover the full lane width. For the forward vehicle collision warning system, detecting a preceding vehicle at a curve with a radius of 250m requires a horizontal FoV of 18°.

- **Angular Resolution**: The angular resolution refers to the minimum angular

distance of two scanning points, which is equivalent to the beamwidth of the laser light. According to the analysis in [1], the horizontal angular resolution is 0.07° on average (over different types and positions of objects) for a distance of 200 m with the detection algorithm of PointPillars [7].

- **Wavelength**: The typical wavelength choices are 905 nm and 1550 nm. The actual wavelength value does not affect the design, as the distance is measured in wavelength.

According to the discussion above, the requirements of LiDAR systems for automotive applications can be summarized as:

- 200 m range of detection
- 18° horizontal field of view
- Horizontal 0.07° wide laser beam

1.2 Optical Phased Array

The LiDAR system can be classified into four types according to the scanning approaches [8]. There are three ways to steer the beam: mechanical rotation, micro-electro-mechanical system (MEMS) and optical phased array (OPA). Among them, the OPA is believed to be the most promising technology and garnered considerable attention from the automotive industry for its fast scanning speed and potential integration on chip. Unlike the physical steering methods, OPAs utilize the wave nature of light and the interference of wavefields to control laser beam directions dynamically. This working principle is the same as phased array radar, steering the beam by manipulating the relative phase of individual antennas. This steering method results in a solid-state LiDAR, a revolutionary departure from traditional mechanical steering methods.

Leveraging Silicon Photonics (SiPh), OPAs can be implemented with silicon-based modules, such as dielectric waveguides, phase shifters, and grating couplers (optical antennas). For this reason, OPAs can be made as photonic integrated circuits (PIC) using fabrication techniques from the semiconductor industry. Therefore, photonic and electronic circuits can be integrated into a single chip. There are several benefits from single-chip OPAs compared to other types of LiDAR systems [4, 9]. Firstly, it reduces the size and weight because it eliminates the bulky mechanical parts. Secondly, avoiding mechanical components offers robustness toward mechanical shocks and vibrations, enabling LiDAR to work in harsh environments. Finally, avoiding expensive optical components, such as lenses, and the compatibility of PIC with existing semiconductor technology dramatically reduces the costs. Single-chip OPAs use the same fabrication process for both photonic and electronic parts. This indicates the whole system can be made on the wafer, reducing the cost of large-scale manufacture.

1.2.1 Architecture and Components of OPA

A typical OPA has the components of the laser source, waveguides, power splitters, phase shifters and grating couplers (optical antennas). The introduction to the working principle of these key components in SiPh is as follows:

- **Waveguides**: Waveguides in OPAs are the part through which optical signal travels. They are akin to the wires in an electrical circuit but for light. These are commonly made from silicon-based dielectric materials in SiPh.

- **Laser source**: A laser source is to provide the optical signal that the OPA manipulates. The choice of the source depends on the structure. 1D OPA requires a tunable laser source to achieve 2D beam steering by adjusting the wavelength, while 2D OPA is capable of 2D single-wavelength beam steering [4, 10].

- **Power splitters**: Power splitters, also known as beam splitters, are devices distributing the optical power among waveguides. There are various types of power splitters, including Y-Splitter and Multi-mode Interferometer (MMI) [2,10]. Both types of power splitters can distribute the optical power equally into two paths, which is commonly required in SiPh OPA architectures.

- **Phase shifters**: Phase shifters are used to control the phase of light in each waveguide by introducing phase delay. Different phase-shifting methods exist, including thermo-optic and electro-optic phase shifters. Despite using thermo or electro effect, the phase shifter works by changing the refractive index of the waveguides. The thermo-optic phase shifter is the most commonly used type because electro-optic phase shifters are typically incompatible with CMOS manufacturing processes, resulting in an expensive implementation. Thermo-optic phase shifters introduce low optical losses with CMOS technology, while the power consumption is up to order of tens and hundreds of milliwatts to perform a π phase shift depending on the materials and designs [11].

- **Grating couplers**: Grating couplers are optical antennas. These components emit the light from the waveguides into free space. It is called the grating coupler due to the element coupling the guided and free-space waves with grating. There are straight waveguide grating couplers and arc grating couplers [12]. Straight waveguide grating couplers are suitable for 1D OPA, and arc grating couplers are suitable for 2D OPA.

Depending on the geometry arrangement, two OPA structures, 1D and 2D, exist. This project will focus on the relevant algorithm for 1D OPAs and leave the 2D OPAs as future work. A schematic diagram of 1D OPAs is shown in Fig.1.4. The 1D OPA uses the straight waveguide grating antenna. By controlling the phases of each grating coupler, the beam can be steered along the direction of θ. Another dimension (ϕ) of steering is achieved by changing the frequency of the laser source [12–14].

Depending on the architecture, the OPA can have additional controls over amplitude so that the OPA can achieve a better performance [10]. This amplitude control can be achieved with the *Mach-Zehnder Modulator* (MZM) as shown in Fig.1.5. It consists

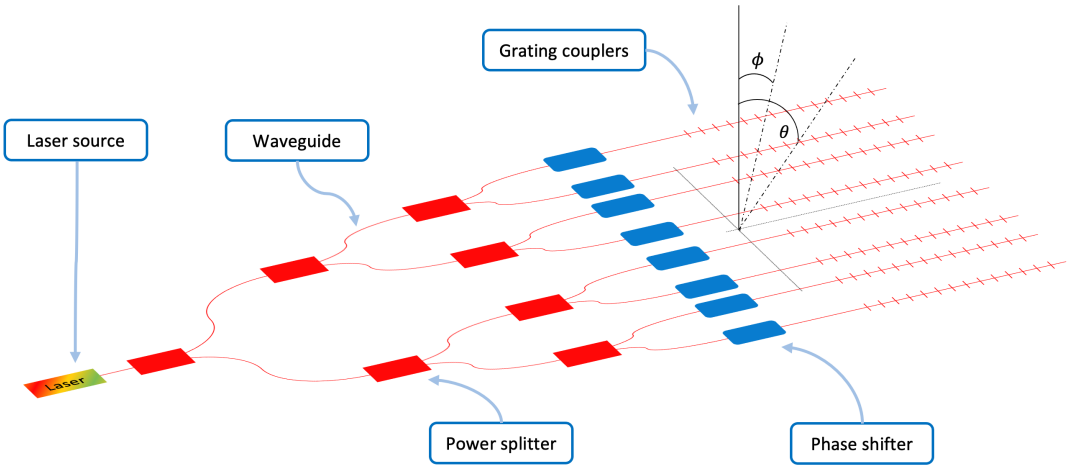

Figure 1.4: The schematic of a typical 1D OPA structure. The beam steering along the θ direction is achieved by applying phase shifts. The beam steering along the ϕ direction is achieved by varying the wavelength.

of an integrated optical interferometer with two branches, where an input light beam is split into two paths that are then recombined. Differently changing the refractive index of the optical paths introduces two phase shifts to the two paths. Depending on the phase difference between the two branches, the recombination is constructive or destructive interference, thus controlling the output intensity and phase. The schematic diagrams of two types of OPA are shown in Fig.1.6, depending on whether there is the capability to control the amplitude. Our work is based on the architecture as shown in Fig.1.6b.

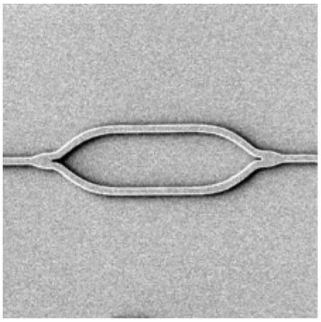

Figure 1.5: A photo of Mach-Zehnder Modulator [2]. MZM modulates the optical signal by changing the refraction index of two branches. The output signal has an amplitude and phase depending on phase shifts and their difference.

1.2.2 Radiation Pattern and Array Factor

In the field of array theory, the concept of the array factor plays a pivotal role in the analysis and design of antenna arrays. It is a fundamental function that quantifies

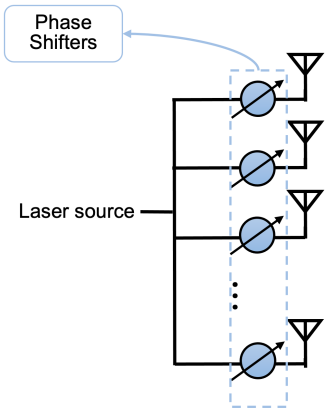

(a) The schematic of OPA with control of phase.

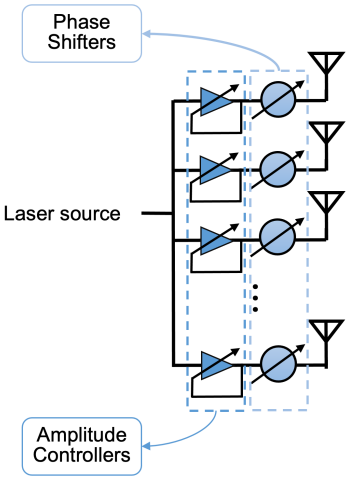

(b) The schematic of OPA with control of amplitude and phase.

Figure 1.6: The schematics of two types of OPA structure. The distinction is the controllability of the excitation amplitude of each antenna.

the collective radiation pattern resulting from the geometric arrangement and phase relationships of individual antenna elements within an array.

Unlike the elemental pattern, which is determined by the physical and electrical properties of a single antenna, the array factor captures the impact of the spatial distribution and phase differences of multiple antennas working accordingly. This interaction significantly influences the overall radiation characteristics, such as beam direction, shape, and width. The array factor, therefore, is integral for antenna arrays to achieve specific radiation objectives, including beam steering, shape control, and sidelobe reduction.

The total radiation pattern of an antenna array is effectively modelled as the multiplication of the individual element pattern and the array factor [15]. The array factor can be seen as the total radiation pattern of an array with only *isotropic radiators*. A single isotropic radiator has a field:

$$w\frac{e^{-jkr}}{r} \tag{1.1}$$

where the w is the excitation (including amplitude and phase), the r is the distance from a point to the isotropic radiator, k is the wavenumber $k = \frac{2\pi}{\lambda}$, and λ is the wavelength.

Considering a geometrical arrangement of placing N isotropic radiators along the x-axis with each location at x_n as shown in Fig.1.7, the total radiation pattern in the xy-plane is:

$$B = \sum_{n=1}^{N} w_n \frac{e^{-jkr_n}}{r_n} \tag{1.2}$$

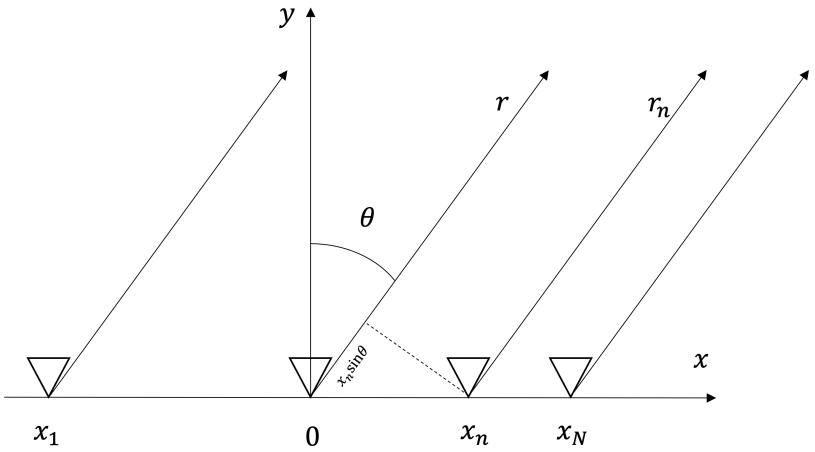

Figure 1.7: The geometry of the array arrangement for this project. The origin is the reference point for the phase shift. Under the far-field assumption, the phase difference between each element and the reference point is due to the $x_n \sin\theta$.

Assuming the field point is in the far field, where the wave is plane, the vectors from each element to the point are approximately parallel. Therefore, $r_n = r - x_n \sin\theta$ and the difference in distance for nth element is $x_n \sin\theta \ll r$. This small difference is neglectable in the denominator of (1.1) and significant for the exponential term in the numerator. Therefore, the (1.2) can be factored out as:

$$B = \frac{e^{-jkr}}{r} \sum_{n=1}^{N} w_n e^{jkx_n \sin\theta} \tag{1.3}$$

The leading term is constant for a given radial distance r. Next to the constant term, the summation is the *array factor*, a function of angle θ. The array factor captures the collective radiation pattern, denoted by:

$$p(\theta) = \sum_{n=1}^{N} w_n e^{jkx_n \sin\theta} \tag{1.4}$$

The above expression of array factor can be written in a vector product form:

$$p(\theta) = \boldsymbol{s}^H(\theta)\boldsymbol{w} \tag{1.5}$$

where $\boldsymbol{s} = [e^{jkx_1 \sin\theta}, e^{jkx_2 \sin\theta}, ..., e^{jkx_N \sin\theta}]^H \in \mathbb{C}^{N\times 1}$ is the *steering vector* and $\boldsymbol{w} = [w_1, w_2, ..., w_N]^T \in \mathbb{C}^{N\times 1}$ is the *excitation vector*.

The array factor has a determining impact on the width of the mainlobe of the overall radiation pattern. It also determines the beam direction for beam steering. In other words, the beamwidth and beam direction of the overall radiation pattern mostly rely on the array factor regardless of the elemental pattern. Therefore, working with the array factor is sufficient for designing a small beamwidth array [15]. Since the array factor is the determining term for array design and beam steering, and we are

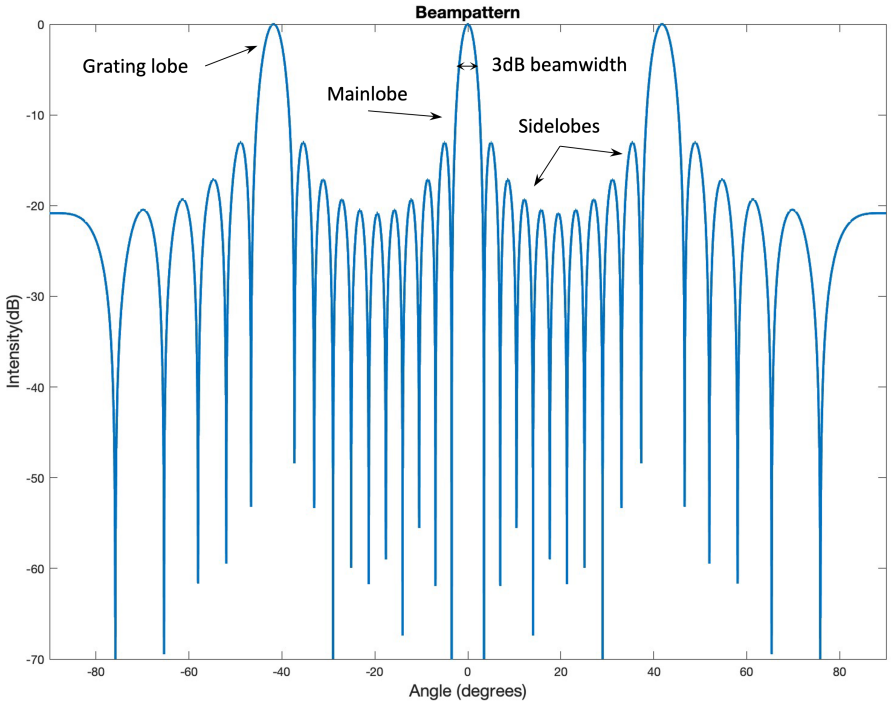

Figure 1.8: An example of beampattern of a uniform spacing linear array with $N = 11$ and spacing of 1.5 wavelength.

also using isotropic radiators, the terms "array factor" and "beampattern" are used interchangeably in the following chapters.

An example of a beampattern is shown in Fig.1.8, where the beampattern is normalized to its maximum value equals 1, allowing the comparison across different designs. Regarding the beampattern, the following concepts are important throughout this project:

- **Mainlobe**: This is the primary lobe of radiation and represents the direction in which the radiation strength is the strongest. The mainlobe is the most significant part of the radiation pattern.
- **Beamwidth**: Beamwidth refers to the angular width of the mainlobe, typically measured between points at which the radiation pattern falls to half its peak value (-3dB points), namely half-power beamwidth. Beamwidth is a critical parameter as it determines the revolving power of the OPA LiDAR system, as explained in Section 1.1.
- **Sidelobes**: There are lobes at angles other than the target direction. Sidelobs are usually undesirable as they represent the power leakage in unwanted directions. The level of sidelobes is a critical factor in array design, as they can cause interference and reduce the system's overall performance.
- **Grating lobes**: Grating lobes have the same intensity as the mainlobe but in unwanted directions. They are essentially replicas of the mainlobe due to the larger

than half-wavelength periodic spacing. Grating lobes are particularly problematic as they project the light with equal intensity into directions more than the target direction, causing ambiguity. An example is given in Fig.1.9. Although the elemental pattern can mitigate this issue in the overall beampattern, this project focuses on designing a beampattern that has no grating lobes over twice the field of view region.

As explained in Section 1.1, an ideal beampattern should have a beamwidth meeting the application requirement with no sidelobe and grating lobe free range twice than required FoV. The existence of grating lobes and too large peak sidelobe levels significantly reduce the resolving power.

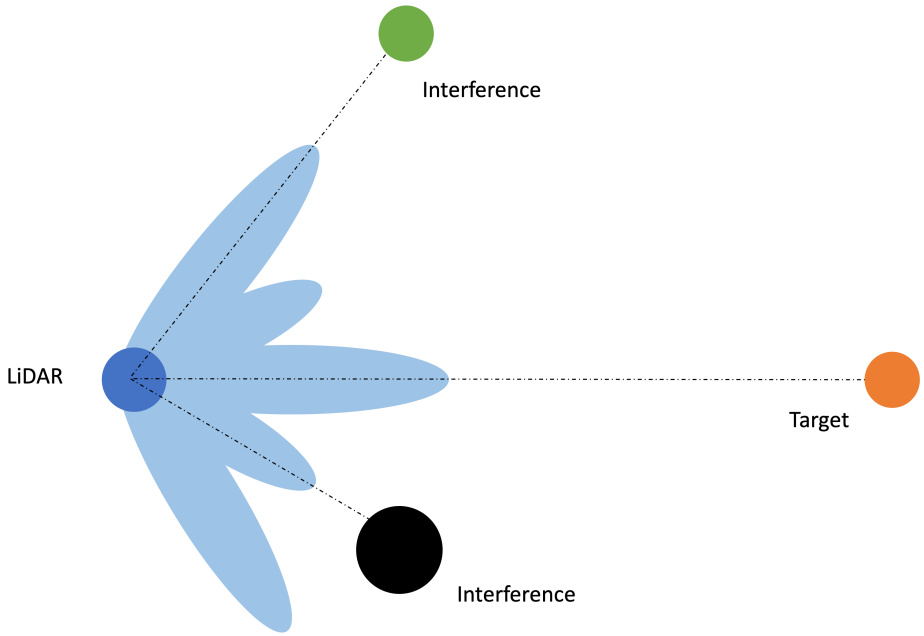

Figure 1.9: The illustration for the effects of grating lobes and sidelobes. The beampattern is illustrated as blue lobes.

An example is shown in Fig.1.9, assuming the OPA LiDAR system generates a beampattern as blue lobes, the interference in green is placed in the direction of the grating lobe and the target in orange is in the direction of mainlobe, and both have the same reflecting ability. In this scenario, the LiDAR receives the reflected beam from the interference first and then the target, with equal intensity, causing ambiguity in determining direction. Additionally, if an interference (in black) with a stronger ability to reflect beam is in the direction of peak sidelobe and closer to LiDAR, it might also cause ambiguity, depending on the level of sidelobe and the ability to reflect. In a word, the grating lobes and sidelobe can reduce the detection performance.

Although the grating lobes exist, a native way to handle it is only using grating lobe free range and steering the beampattern within half of this range. A physical obstacle can block the emission of the unwanted part of the beampattern, allowing only the

desired beam out. This also leads to the definition of the field of view of a beampattern as half of the maximum grating lobe free range.

1.2.3 Performance Metrics

Based on the above discussion, the metrics to assess the performance of resulting sparse OPA designs are summarized as:

- The beamwidth of the mainlobe of the beampattern
- The peak sidelobe level
- The field of view of the beampattern, defined as the half of the grating lobe free region
- The number of elements required to generate the beampattern

1.2.4 Beam Steering

The phased array provides the advantages of beam steering by phase shifting. By timing these phase shifts, the waves from different elements constructively interfere in a desired direction, effectively 'steering' the beam. This method allows for rapid and precise adjustments of the beam's orientation without the need for physical movements of the antenna array.

Recall that the expression of the array factor is:

$$p(\theta) = \sum_{n=1}^{N} w_n e^{j\psi_n} \tag{1.6}$$

where $\psi_n = kx_n \sin\theta$ denoting the phase shift of n-th element. The peak of the main beam is the maximum value of the array factor, which occurs when radiations from all n elements are constructive adding, $\psi_n = 0$ for all n. The peak can be steered by adding phase shift, δ_n, to ψ_n. For the linear array with the geometrical arrangement as shown in Fig.1.7, the phase of n-th element is

$$\psi_n = kx_n \sin\theta + \delta_n \tag{1.7}$$

To steer the main beam to the target direction, θ_t, the δ_n should be selected so that $\psi_n = 0$ at $\theta = \theta_t$. Therefore,

$$\delta_n = -kx_n \sin\theta_t \tag{1.8}$$

This phase shift is linearly progressive along the x axis.

For a set of excitations, $\boldsymbol{w}$, generating a beampattern, steering this beampattern to the direction of θ_t can be written as

$$p(\theta) = \boldsymbol{s}^H(\theta)(\boldsymbol{w} \circ \boldsymbol{\delta_t}) \tag{1.9}$$

where $\boldsymbol{\delta_t} = [e^{\delta_1}, ..., e^{\delta_N}]^T \in \mathbb{C}^{N\times 1}$ collects the progressive phase shifts and $\circ$ is the Hadamard product.

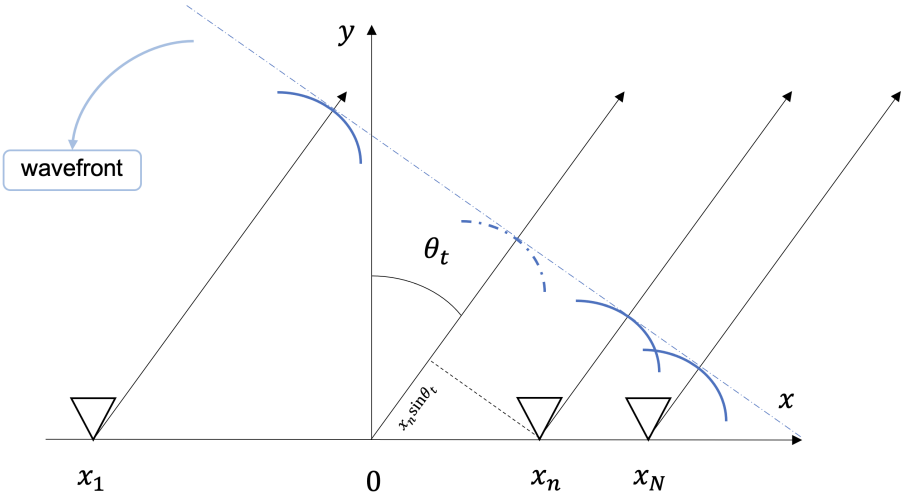

Figure 1.10: The schematic diagram of beam steering, where the origin is phase reference

1.2.5 Motivations for Sparse and Non-uniform Spaced OPA

Automotive applications require a beampattern with a small beamwidth. According to the Rayleigh criterion, the resolving power, namely angular resolution, of a system is determined by the wavelength and aperture:

$$\Delta\theta \approx \frac{1.22\lambda}{D} \tag{1.10}$$

where $\Delta\theta$ is the minimum resolvable distance in radians, λ is the wavelength of light, and D is the aperture diameter. The angular resolution in OPA is the beamwidth of the mainlobe. Therefore, the beamwidth of the mainlobe is only determined by the aperture and the working wavelength.

1.2.5.1 Uniform Linear Array with Half-wavelength Spacing

To form such a beampattern, the most naive solution is to use a uniform linear array (ULA), meaning an array with uniformly spaced identical antenna elements arranged along a line, with half-wavelength elemental spacing to cover the required aperture. The reason for this spacing is that the half-wavelength spacing guarantees that no grating lobe appears in the beampattern. As shown in Fig.1.11a, the mainlobe's beamwidth decreases with the number of elements increases.

However, this naive solution is infeasible for an optical phased array design that meets the required beamwidth. The half-wavelength spacing is too small in the optical application, and the number of necessary elements is large, causing challenges in power storage and cooling of the system. According to the Rayleigh criteria, achieving an angular resolution of 0.07° requires an array aperture up to 1000λ. For a ULA with half-wavelength spacing, the total number of elements required to cover such an aperture is 2000. The phase shifters use the thermo-optic effect, namely heating, to alter the

phase for each element. 2000 elements mean power consumption of around 10 Watts for only the phase shifting part, given 9.6 mW for a π phase shift [16] and assuming a linear relationship between power and phase shifts with uniform distribution over [0,2π]. Using Mach-Zehnder Modulators (introduced in Section 1.2.1) for amplitude control in OPAs necessitates phase shifters, thereby further increasing total power consumption. Such power consumption poses a challenge to energy storage for automotive applications. Moreover, given a working wavelength of 1550 nm, the physical length of this array is around 1.55 mm. Such an amount of heat generated in this small area also poses a challenge to the cooling of the system.

The half-wavelength spacing also causes interference between waveguides, namely crosstalk, in OPAs. The OPAs use dielectric waveguides, which are hard to confine electromagnetic waves compared to metals used in RF. Although effects have been done on materials, the spacing larger than half-wavelength helps reduce crosstalk dramatically [17, 18]. Therefore, the minimum spacing for OPA is set to be one wavelength.

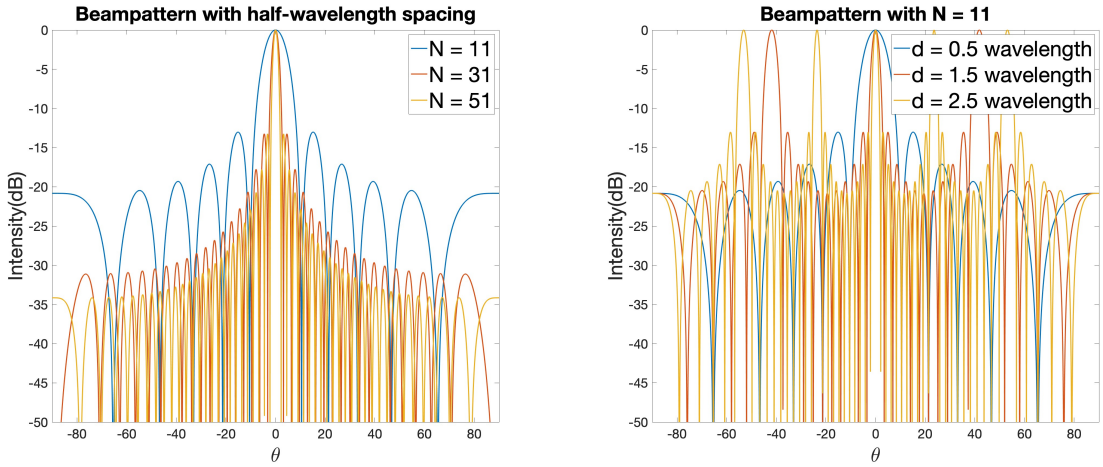

(a) The beampatterns with increasing number of elements

(b) The beampatterns with increasing elemental spacing

Figure 1.11: The beampatterns of achieving the same aperture by only increasing the number of elements and only increasing the elemental spacing.

1.2.5.2 Sparse and Non-uniform Array Configuration

To address the issue of power consumption, employing fewer elements to cover the necessary aperture is beneficial. By increasing the uniform spacing between elements, as illustrated in Fig.1.11b, the same aperture can be achieved with larger spacing and fewer elements, which maintains the beam pattern's mainlobe beamwidth. Importantly, the decrease in the number of elements leads to reduced power consumption, mitigating heating problems. Meanwhile, this large uniform spacing design mitigates the crosstalk issue by increasing the distance between waveguides.

However, the trade-off is the reduced field of view due to the grating lobes. Shown in Fig.1.11b, the field of view almost halved when the spacing increased from 1.5 to 2.5

for a slightly narrower beamwidth. To perform a range detection of target direction without ambiguity (Fig.1.3), no grating lobe must appear in the field of view when steering the beam. Therefore, the useful part of the beampattern is smaller since the grating lobes appear. This is unavoidable due to the periodic appearance of elements.

The problem of reduced FoV can be mitigated with an aperiodic spatial arrangement of elements, resulting in a non-uniform linear array [18, 19]. The above description for the desired OPA fits the definition of the counterpart in the antenna community, sparse array antenna, according to the "IEEE Standard for Definitions of Terms for Antennas" [20]. The definition of sparse array antenna highlights three characteristics:

- Substantially fewer elements than conventional uniformly spaced array
- Same beamwidth with the conventional uniformly spaced array
- Interelement spacings can be chosen so that no grating lobes and sidelobes issues arise

By definition, the last characteristics of sparse array antenna implies a non-uniform element spacings. In other words, non-uniform spacing is not the requirement but a means to achieve a beampattern that meets the requirement. We apply the same definition to our OPA design problem. Thus, automotive applications require a sparse OPA to generate a beampattern that meets the angular resolution for collision avoidance with fewer elements involved.

In summary, fulfilling the requirements of automotive applications using a uniform linear array with half-wavelength spacing is not feasible. Therefore, the sparse optical phased array emerges as the optimal solution. By reducing the number of elements and associated phased shifters, it significantly lowers power consumption, facilitates cooling of the LiDAR system, minimizes crosstalk between waveguides, and expands the field of view compared to a uniform OPA. Thus, the goal is to identify an optimal sparse OPA configuration that meets specific design requirements, such as beamwidth and field of view.

1.3 Literature Review

The prior works address the general sparse OPA design problem, including various hardware architectures and design strategies. For example, a work of designing a 2D sparse OPA with only phase control by removing elements on a 2D grid [10] and another work of designing a 1D sparse OPA with full excitation control by moving elements on a continuous line [21]. To systematically analyze the existing literature, three binary classification criteria are used:

- 1D architecture or 2D architecture
- With or without controllability of excitation amplitude
- Positions of elements can be on a grid (finite and discrete) or off-grid (infinite and continuous)

These three binary criteria classify the sparse OPA design problem into 8 categories. Every prior work can be classified into one and only one category.

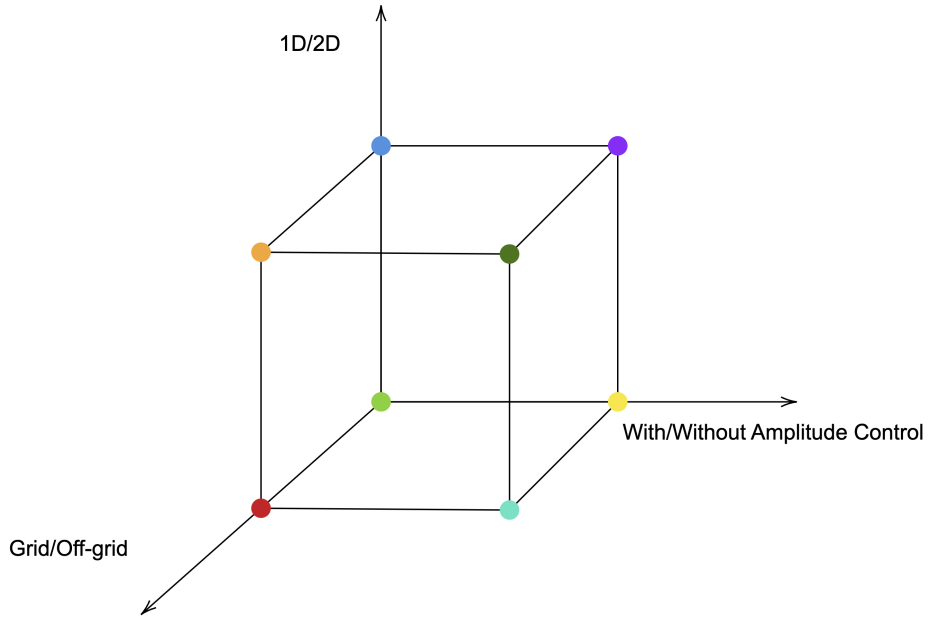

Figure 1.12: A visualization of 3D binary classification of the OPA design problem

Architecture	Grid	Off-Grid
1D Amplitude Control	This project	[21]
1D No Amplitude Control		[22–25]
2D Amplitude Control		
2D No Amplitude Control	[10]	

Table 1.1: The classification of all OPA architectures and the corresponding algorithm to solve the sparse OPA design problem.

1.3.1 Algorithms

Despite the difference in OPA architecture, the primary algorithms used in sparse OPA design are evolutionary algorithms, including the genetic algorithm (GA) and particle swarm optimization (PSO). Both algorithms are inspired by biological evolution: GA simulates natural selection by encoding the parameters into various individuals (candidate solutions) and randomly explores the solution space through crossover and mutation. PSO represents parameters within a solution space, using moving particles to seek the optimal solution. In essence, evolutionary algorithms engage multiple entities (individuals or particles), each representing a potential solution, to explore the solution space randomly. This search method is designed to identify the global optimal solution.

For sparse OPA design challenges, the elemental position, x_n, features in the exponential term of (1.4), making direct optimization against element position or spacing nonlinear. Evolutionary algorithms are well-suited for such nonlinear problems, as they do not require a gradient. Consequently, the majority of algorithms for sparse OPA

design employ either GA [10, 22–24] or PSO [21, 25].

However, evolutionary algorithms do not ensure the discovery of the optimal solution, a problem exacerbated by high-dimensional problem spaces. Both GA and PSO depend on deploying numerous entities within the solution space to achieve adequate coverage. In OPA design, where parameter counts may reach 1000, the curse of dimensionality dictates that an extensive number of entities is required to thoroughly search the space for the optimal solution, challenging the effectiveness of GA and PSO in finding the optimal solution.

Furthermore, existing works face limitations in configuring sparse OPAs. Algorithms that encode elemental spacings fix the number of elements [21–25], complicating the task of identifying an OPA configuration with the minimum necessary elements to meet specified beampattern performance criteria. While encoding active status and incorporating solution sparsity into the fitness function [10] can enhance the search for sparse solutions, it does not offer precise control over the sparsity of the outcomes.

1.4 Research Question

The discussion above reveals a significant gap in sparse OPA design research: existing algorithms struggle to efficiently identify the sparsest OPA configuration (minimum number of elements) that satisfies desired beampattern characteristics (e.g., beamwidth and field of view) while maintaining element spacing above a specified threshold.

Consequently, this project poses the following research question: How can the sparsest OPA configuration be identified to meet the requirements of automotive applications?

2 Problem Formulation

In this chapter, we present the methods used to formulate the research objective as an optimization problem. These methods address two main challenges: mathematically describing the constraints related to the beampattern and quantifying the sparsity level of a sparse OPA. Ultimately, the research objective is formulated as the best subset selection of the excitations. This formulation bypasses the nonlinearity associated with directly optimizing the positions of elements, thus simplifying the problem. We then introduce several algorithmic techniques from the field of compressive sensing that have been effective in deriving sparse solutions. Employing these techniques allows us to address the sparse OPA design challenge and achieve the desired sparse OPA configurations.

2.1 Sparse OPA Design

The OPA is still an antenna array, to which the general array design theories apply. Various useful methods exist in array design, including array thinning, array synthesis, and the combination of these two methods known as sparse array synthesis. Array thinning bypasses the nonlinearity associated with determining an element's position within a sparse array. This is achieved by deactivating elements within a ULA, restricting element positions to a predefined grid, rather than a continuous range. Array synthesis, on the other hand, provides a means of obtaining the excitations needed for an array to produce a beampattern that satisfies specific metrics. Sparse array synthesis integrates the concept of array thinning into array synthesis, offering an efficient approach to achieving a sparse array configuration using a grid. The following sections will provide a more detailed explanation of these concepts.

2.1.1 Array Thinning

Array thinning is an approach to achieve a sparse array by deactivating elements within a ULA. Recall the expression of array factor (1.4), where the elemental position, x_n, is a factor in the exponential function. Consequently, the beampattern has a nonlinear dependency on elemental position, complicating the geometric design of the antenna array. Array thinning bypasses this challenge by using a grid (as represented by the ULA) to discretize x_n's continuous range into a finite set of candidate positions. As a result, the sparse array design problem is transformed into the task of selecting a subset of these candidate positions. The discretization inherent in this grid-based approach results in element spacings that are multiples of the grid spacing, effectively establishing a minimum spacing requirement for the resultant sparse array configuration.

An example is thinning an N-element ULA with uni-norm excitation, where the

phase is adjusted to peak in the desired mainlobe direction, θ_t. This adjustment effectively represents a progressive phase shift along the x-axis. By substituting $w_n = e^{-jkx_n \sin\theta_t}$ into (1.4) and introducing a binary selecting term, $a_n \in \{0, 1\}$, for each element, the beampattern can be expressed as:

$$p(\theta) = \sum_{n=1}^{N} a_n e^{jkx_n(\sin\theta - \sin\theta_t)} \tag{2.1}$$

Thinning an array to enhance the beampattern—particularly to reduce peak sidelobe levels and minimize grating lobes—poses a combinatorial optimization challenge. This approach results in sparse array configurations.

2.1.2 Array Synthesis

The concept of array synthesis plays a pivotal role in antenna design [15]. Its primary goal is to engineer an antenna array with excitations that yield a beampattern possessing specific characteristics. Array synthesis first requires a model to represent these desired characteristics approximately, such as small beamwidth and low sidelobe level. Subsequently, the objective is to match the beampattern of the actual array model,—represented by the array factor as defined in (1.4)—with the desired beampattern. In essence, array synthesis methods design arrays whose array factors approximate the desired beampattern.

The matching between the desired and the generated beampatterns is typically executed across a finite set of sampling points within the specified region of interest, $[\theta_{min}, \theta_{max}]$, with the remaining portion of $[-\pi, \pi]$ designated as "don't care" regions. This region of interest is twice the field of view, ensuring that grating lobes remain absent within this critical area. An example of the desired beampattern is illustrated in Fig.2.1, in which the pencil shape beam indicates the ideal beamwidth and the ideal sidelobe level is 0. Consequently, the array synthesis method poses the requirements for beampattern in the resulting array configuration.

Using a uniform sampling strategy across $[\theta_{min}, \theta_{max}]$, we define a set of L sampling points of θ as follows:

$$\Theta = \{\theta_l | \theta_l = \theta_{min} + \frac{l-1}{L-1}(\theta_{max} - \theta_{min}), l = 1, ..., L\} \tag{2.2}$$

The value of L should be chosen to guarantee the sampling interval is less than half of the beamwidth, well capturing the characteristic of beamwidth. This requirement can be interpreted as a natural extension of the Nyquist sampling theorem. Given an analytical function $p_d(\theta)$ defined on $[\theta_{min}, \theta_{max}]$ that describes the characteristics such as beamwidth and sidelobe level, the matching between the physical model and the desired beampattern is performed over L sampling points. For a N-element linear array, the expression for the array factor in vector product form is (1.5). Thus, the matching between the desired and generated beampattern results in L equations:

$$p_d(\theta_l) = \boldsymbol{s}^H(\theta_l)\boldsymbol{w} \qquad l = 1, ..., L \tag{2.3}$$

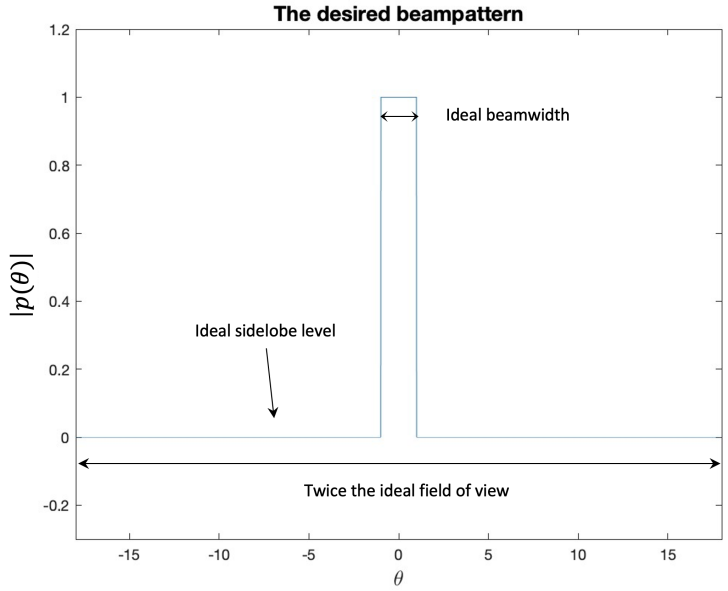

Figure 2.1: An example of the desired beampattern. It captures all requirements regarding the beampattern, including beamwidth, field of view, and ideal sidelobe level.

These L equations form a system of linear equations that can be written in a matrix product form. Define a desired beampattern vector that collects the samplings of the desired beampattern:

$$\boldsymbol{p}_d = \begin{bmatrix} p_d(\theta_1) \\ p_d(\theta_2) \\ \vdots \\ p_d(\theta_L) \end{bmatrix} \in \mathbb{C}^{L\times 1} \tag{2.4}$$

and a *steering matrix* stacking multiple steering vectors

$$\boldsymbol{S} = \begin{bmatrix} - & \boldsymbol{s}^H(\theta_1) & - \\ - & \boldsymbol{s}^H(\theta_2) & - \\ & \vdots & \\ - & \boldsymbol{s}^H(\theta_L) & - \end{bmatrix} \in \mathbb{C}^{L\times N} \tag{2.5}$$

Therefore, the system of equations is a matrix equation

$$\boldsymbol{p}_d = \boldsymbol{S}\boldsymbol{w} \tag{2.6}$$

where the desired pattern vector $\boldsymbol{p}_d$ is known, $\boldsymbol{S}$ is known once the working wavelength and the array's geometry are known. The complex excitation vector $\boldsymbol{w}$ is the only unknown in (2.6). Thus, the array synthesis problem can be interpreted as an inverse problem, determining an excitation vector $\boldsymbol{w}$ with given $\boldsymbol{p}_d$ and $\boldsymbol{S}$.

Since the desired beampattern is usually ideal (sidelobe level is 0), a perfect match on all sampling points is impossible. This infeasibility means the system of linear equations is inconsistent, for which a least square solution for the excitation vector

$\boldsymbol{w}_{LS}$ can be found. For example, given an array ($\boldsymbol{S}$) and a desired beampattern ($\boldsymbol{p}_d$), the least square solution $\boldsymbol{w}_{LS}$ is the best in the sense of resulting in the minimum error $\|\boldsymbol{S}\boldsymbol{w}_{LS} - \boldsymbol{p}_d\|_2$, the Euclidean distance in the pattern space, $\mathbb{C}^L$.

2.1.3 Sparse Array Synthesis

Array thinning results in a sparse array configuration and imposes the minimum spacing requirement on the result, while array synthesis imposes the requirements regarding the beampattern. Thus, combining the idea of the array thinning method with the array synthesis approach results in the sparse array synthesis method. This method can accommodate all requirements and constraints for the resulting sparse array configuration, including beamwidth, field of view, sidelobe level, and minimum spacing. Sparse array synthesis deactivates elements by setting the corresponding excitation w_n to zero. This approach uses an excitation vector $\hat{\boldsymbol{w}}$ to determine a subset of the ULA and the corresponding excitations to generate the optimal beampattern [26–28].

Therefore, the research objective of this project, described in Section 1.4, can now be addressed by the sparse array synthesis method, seeking a set of excitations for a ULA that maximizes the number of zeros given a desired beampattern. We now express the above problem statement mathematically as follows:

$$\begin{aligned} &\underset{\boldsymbol{w}\in\mathbb{C}^N}{\operatorname{argmin}} \|\boldsymbol{w}\|_0 \\ &\text{s.t.} \quad \|\boldsymbol{S}\boldsymbol{w} - \boldsymbol{p}_d\|_2 \leq \epsilon \end{aligned} \tag{2.7}$$

where $\|\cdot\|_0$ is the l_0-norm defined as the number of nonzero entries of a vector, and $\epsilon \geq 0$ determines the maximum permissible error between generated and desired beampatterns. This problem formulation utilizes a grid to obtain the sparsest OPA configuration by minimizing the number of nonzero entries in the excitation vector $\boldsymbol{w}$ given that the deviation of the generated beampattern from the desired one is less than what ϵ determines. This formulation ensures the minimum spacing by using a grid and imposes all the requirements regarding beampattern with the constraint of $\|\boldsymbol{S}\boldsymbol{w} - \boldsymbol{p}_d\|_2 \leq \epsilon$. The notation $\boldsymbol{w} \in \mathbb{C}^N$ indicates that the solution represents an OPA structure with amplitude control (as depicted in Fig:1.6b), which is the focus of this project.

The above formulation (2.7) is essentially a best subset selection problem, recognized nonconvex and NP-hard [29]. Although exhaustive search may be feasible for small-scale problems, the efficiency decreases when the problem has a large N. The OPA design problem has a value of N up to thousands, further complicating the issue. Fortunately, algorithmic advancements within the compressive sensing paradigm have facilitated effective and efficient solutions to the problem (2.7) based on the sparse array synthesis method. The next section will introduce the algorithms that effectively and efficiently solve this problem.

2.2 Sparsity-Promoting Algorithm

Over the last few decades, compressive sensing (CS) has developed significantly in signal processing and applied mathematics. The CS theory states certain signals can be

reconstructed from fewer samples than those required by the Nyquist-sampling strategy, sensing signals in a compressed fashion, as its name implies. The CS framework consists of two parts: the theory of sampling scheme design to enable recovery and the algorithms to reconstruct sparse solutions. These sparse recovery algorithms, which promote sparsity and reconstruct the sparse solution, are at the heart of CS. As the name implies, sparse recovery algorithms emphasise recovering a signal known to be sparse as prior. However, the task in this project is to design the sparsest array without prior knowledge of the solution, making the term "recovery" somewhat imprecise. Hence, we refer to it as *sparsity-promoting algorithms* to emphasise that the algorithm enforces sparse solutions. Typical sparsity-promoting algorithms include Basis Pursuit and its variants line LASSO [30], Thresholding Algorithms, and Greedy Algorithms like Orthogonal Matching Pursuit. The following sections will present the useful algorithms for our problem formulation.

2.2.1 LASSO Problem

Among these algorithms, the basis pursuit algorithm, particularly its variant LASSO, is our focus. The LASSO problem is a method of regression analysis that shrinks coefficients and sets some to zero. Unlike solving problem (2.7) with an l_0-norm, LASSO solves the problem with an l_1-norm, serving as the convex relaxation of the l_0-norm. Therefore, the research objective to find the sparsest OPA that meets the requirements as in Section 1.1 is formulated as:

$$\begin{aligned} &\underset{\boldsymbol{w}}{\operatorname{argmin}} \|\boldsymbol{w}\|_1 \\ &\text{s.t.} \quad \|\boldsymbol{S}\boldsymbol{w} - \boldsymbol{p}_d\|_2 \leq \epsilon \end{aligned} \tag{2.8}$$

where $\|\boldsymbol{w}\|_1 = \sum_{n=1}^{N} |w_n|$, $\boldsymbol{p}_d$ encapsulates the beampattern characteristics, $\boldsymbol{S}$ ensures the minimum spacing, ϵ determines the largest allowable matching error.

The geometrical interpretation of problem (2.8) is shown in Fig.2.2a using a two-dimensional example. The rectangle represents $\|\boldsymbol{w}\|_1$, and the elliptical contours are $\|\boldsymbol{S}\boldsymbol{w} - \boldsymbol{p}_d\|_2$ at different values. The centre of the elliptical contours is the least square solution, $\hat{\boldsymbol{w}}_{LS}$, attending the minimum error for $\epsilon_{LS} = \|\boldsymbol{S}\hat{\boldsymbol{w}}_{LS} - \boldsymbol{p}_d\|_2$. In the form of (2.8), minimizing $\|\boldsymbol{w}\|_1$ shrinks the rectangle, and ϵ defines the largest permissible ellipse. An increasing ϵ enlarges the ellipse and contracts the rectangle. Therefore, the optimal solution for a given ϵ is the intersection of the smallest rectangle and the largest ellipse, yielding the minimum l_1-norm solution. Due to the geometry of the l_1-norm, the optimal solution will most likely be at the rectangle's corners, promoting zero coefficients. This effect contrasts with the l_2-norm scenario (Fig.2.2b), where solutions seldom contain zero entries due to the shape of l_2-norms (the circle represents $\|\boldsymbol{w}\|_2$).

This example highlights the shrinkage nature of the LASSO problem, which can be generalized to high-dimensional space. Therefore, the problem of (2.8) is expected to provide the sparsest solution for a specified ϵ. By tuning the hyperparameter ϵ, the LASSO problem trades the matching quality for the coefficients' sparsity. Two extreme examples are: Firstly, too large ϵ allows a very loose matching, then the $\|\boldsymbol{w}\|_1$ shrinks to zero, meaning an array without elements. The error term reach its maximum of $\epsilon_{max} = \|\boldsymbol{p}_d\|_2$ when the $\boldsymbol{w} = \boldsymbol{0}$. Secondly, an overly restrictive ϵ (for example, $\epsilon = 0$)

results in an infeasible problem because the exact match is impossible. The smallest feasible ϵ_{LS} is given by the least square solution, which falls to promote sparsity, as we will show in the next chapter. Therefore, the meaningful range of ϵ is $[\epsilon_{LS}, \epsilon_{max}]$. Since the problem (2.8) is convex, the off-the-shelf solver can efficiently solve this problem. For this project, we employed CVX to solve this LASSO problem [31, 32].

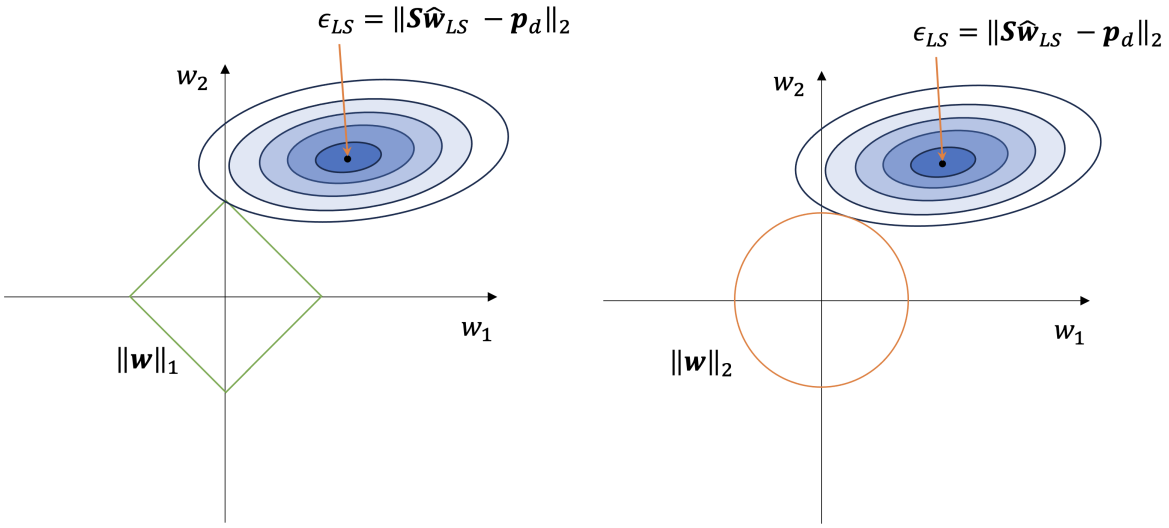

(a) The geometrical interpretation of the LASSO problem where a l_1-norm is used. Due to the shape of l_1-norm ball, the solution tends to have zero entries.

(b) The geometrical interpretation of the Ridge problem where a l_2-norm is used. Due to the shape of l_2-norm ball, the solution tends to have only nonzero entries.

Figure 2.2: The geometrical interpretation of LASSO and Ridge problem, in which the difference is the norm used. The centre of the elliptical contour is the least square solution.

2.2.2 Thresholding

As we will see in Section 3.3, the solution to the LASSO problem is not always as sparse as expected. This might be attributed to the properties of matrix $\boldsymbol{S}$, which plays a crucial role in CS problems. Generally, in CS problems, the matrix is designed to process properties that enable sparse recovery following measurements acquisition. This manipulation of $\boldsymbol{S}$ is achieved through proper sampling schemes. However, in this project, the matrix $\boldsymbol{S}$ is predetermined by the grid and sampling strategy of the desired beampattern at the beginning, making efforts for improvement challenging.

Given the matrix $\boldsymbol{S}$ is fixed by the formulation of the problem, one intuitive approach is to apply another type of sparsity-promoting algorithm, thresholding, to sparsify the results of LASSO problem, denoted as $\hat{\boldsymbol{w}}$. The thresholding algorithm retains the k largest entries to yield a k-sparse solution, $\hat{\boldsymbol{w}}_k$. A detailed analysis of the effects of thresholding on the beampattern will be conducted in the next chapter. A general observation is that as more of the smallest entries are removed from $\hat{\boldsymbol{w}}$, the overall sidelobes of the beampattern are elevated, while the mainlobe remains almost unaffected. This overall elevation of the sidelobe region can be interpreted as immersing

the beampattern in a noise-like floor. Yet, this elevation process stops once the number of nonzero entries is significantly reduced. If k is too small, there is a substantial alteration in the shape of the mainlobe. Therefore, thresholding the results of the LASSO problem allows for the exploration of the smallest k that results in a beampattern fulfilling the performance requirements, trading off the performance of the beampattern for the reduction in the number of elements.

2.2.3 Reweighted l1-norm Minimization

As the formulation of (2.8) fails to deliver sparse solutions, the question of whether the l_1-norm properly approximates the behaviour of l_0-norm arises. It is necessary to revisit the usage of l_1-norm as the approximation for l_0-norm. Although the l_1-norm is the best convex approximation for l_0-norm, their difference is not neglectable. Minimizing the l_0-norm equally penalizes all nonzeros entries, while reducing the l_1-norm more heavily penalizes large entries. The illustration of the difference from a geometrical perspective is shown in Fig.2.3.

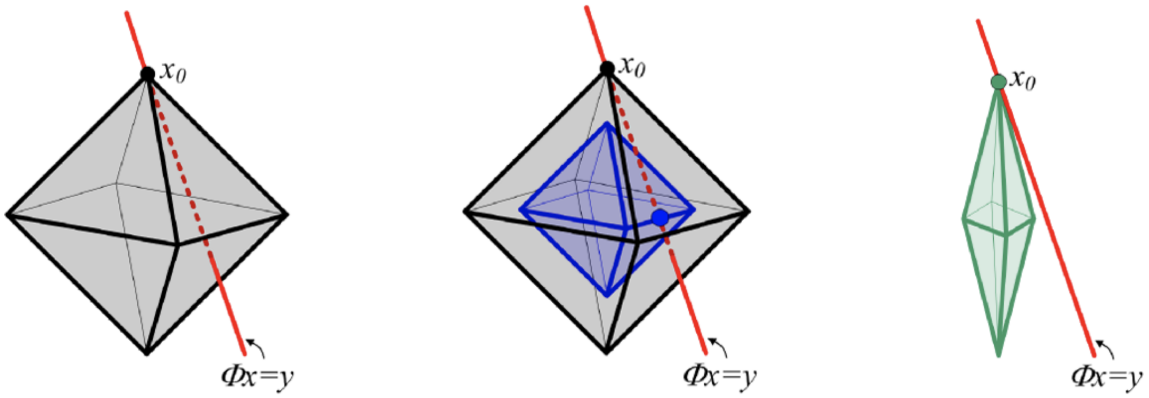

(a) (b) (c)

Figure 2.3: An 3D illustration of weighting l_1-norm minimization to enhance the sparsity of solution [3]. a) Sparse solution x_0 with one nonzero entry is the intersection between the feasible set (red line) and the $\|x_0\|_1$. b) A solution $x \neq x_0$ with two nonzero entries exists for which $\|x\|_1 < \|x_0\|_1$. c) Weighted l_1-norm ball. No solution $x \neq x_0$ for which $\|\Gamma x\|_1 \leq \|\Gamma x_0\|_1$

To bridge this difference between two norms, an iterative reweighted l_1-norm minimization better mimics the l_0-norm and enhances sparsity [3]. The core principle of this approach involves iteratively reweighting the l_1-norm of the excitations, assigning lower weights to larger coefficients and higher weights to smaller coefficients. This iterative reweighting process effectively encourages the algorithm to minimise the smaller coefficients, leading to a sparser solution. The algorithm of iterative reweighted l_1-norm minimization is described as Algorithm 1.

The reweighted l_1-norm approach alters the shape of l_1-norm ball as Fig.2.3c. Thus, it produces solutions closer to the true l_0-norm minimization, which directly targets sparsity but is computationally intractable for large-scale problems. By iteratively updating the weights and solving a series of weighted l_1-norm minimization problems,

the reweighted l_1-norm method efficiently enhances the sparsity of the solution. As we will see in the next chapter, this iterative reweighted l_1-norm minimization promotes sparse solutions meeting our research goal.

Algorithm 1: Iterative Reweighted l_1-norm Minimization

Input: Desired beampattern $\boldsymbol{p}_d$, Steering matrix $\boldsymbol{S}$, Hyperparameter ϵ, Number of iterations M, Stability term α, Diagonal weighting matrix $\boldsymbol{\Gamma}$ with $\gamma_1, ..., \gamma_N$ on the diagonal and zeros elsewhere.

initialize $\boldsymbol{\Gamma}^1 = \mathbf{I}_N$;

for $m \leftarrow 1$ **to** M **do**

$\hat{\boldsymbol{w}}^{(m)} = \text{argmin}_{\boldsymbol{w}} \ \|\boldsymbol{\Gamma}^{(m)}\boldsymbol{w}\|_1 \quad \text{s.t. } \|\boldsymbol{p}_d - \boldsymbol{S}\boldsymbol{w}\|_2 \leq \epsilon$

$\gamma_n^{m+1} = \frac{1}{|\hat{w}_n^{(m)}|+\alpha} \quad \text{for } n = 1, 2, ...N$

Output: The optimal set of excitations $\hat{\boldsymbol{w}}^{(M)}$

2.3 Summary

This chapter introduced the methods utilized in this project and accordingly formulated our research objective into an optimization. Following the mathematical formulation of the research objective, we introduced some useful techniques from compressive sensing to solve the problem.

We began by detailing the method of sparse array synthesis and explaining how this approach copes with the requirements and constraints of sparse OPA design problems. Subsequently, we formulated the OPA design challenge as the best subset selection problem, as indicated in (2.7), essentially identifying the sparsest OPA configuration through the determination of the sparsest excitation vector for a ULA. This formulation essentially identifies the sparsest OPA configuration by determining the sparsest excitation vector of a ULA. The LASSO problem applies a convex relaxation to the original nonconvex cost function, transforming the problem (2.7) into (2.8). The LASSO, being convex, allows for finding a globally optimal solution. However, as will be discussed in the next chapter, the LASSO problem did not meet our objectives. A thresholding algorithm was then implemented as a remedy for the LASSO problem's failure, promoting sparsity based on the LASSO results. We also revisit the differences between the two norms employed, clarifying the reasons for the LASSO problem's inadequacy. To more accurately approximate the l_0-norm, we employed a reweighted l_1-norm minimization algorithm. The simulation results of these algorithms will be presented in Chapter 3.

3 Results and Analysis

In the previous chapter, we formulated the research question, finding the sparsest OPA that meets the requirements of automotive applications as a best subset selection problem and introduced algorithms that solve this problem.

In this chapter, we present the results of previously formulated problems and analyze them as solutions for solving a mathematical problem and for designing sparse OPAs for automotive applications.

3.1 Simulation Setups

The simulation is performed with parameters specified as:

- The grid spacing is set to one wavelength.
- The number of grid points is set to $N = 1100$.
- The function of the desired pattern is defined on $[-18°, 18°]$ as:

$$p_d(\theta) = \begin{cases} 0 & \text{otherwise} \\ 1 & |\theta| \leq 0.035° \end{cases} \tag{3.1}$$

- The number of samplings on the beampattern is set to $L = 1100$.

The one wavelength spacing is to meet the minimum spacing requirement, preventing crosstalk. Despite the capability of a one-wavelength spaced ULA to be grating lobe free over a wider FoV of $[-90°, 90°]$, we maintain this spacing to allow the algorithms to selectively deactivate elements. This approach forms a sparse array configuration by using only the necessary elements, with the dense grid enabling a finer selection of candidate positions for optimal performance. In other words, the one wavelength spacing is the finest grid that prevents the crosstalk between waveguides.

With the given grid spacing, the number of grid points is set to $N = 1100$ so that the total coverage of the grid is greater than the aperture required by the Rayleigh Criterion (1.10). By having a grid covering the required aperture, the desired beamwidth is guaranteed to be achievable.

The desired pattern is defined to capture the ideal characteristics of the radiation pattern, such as beamwidth, FoV, and sidelobe level, over an angular range of $[-18°, 18°]$, double the required FoV. This 'pencil beam' pattern focuses the OPA's projection narrowly, akin to the sharp focus of a pencil's point, directing the laser light precisely at the target. With the given desired pattern, the number of samplings is set to $L = 1100$ so that the sampling interval on the pattern is smaller than the desired

beamwidth. This guarantees the characteristic of the beampattern is well captured in terms of beamwidth.

The parameters above are necessary to simulate the results for (2.7). The interpretation of the simulations with these parameters is finding a sparse OPA configuration from an 1100-point grid. The grid spacing is set to meet the minimum spacing requirement. This configuration generates a beampattern matching the desired beamwidth and sidelobe level.

3.2 Framework of Analysis

The solution to the previously formulated problem is $\hat{\boldsymbol{w}}$, the excitation vector. This vector indicates where and how much power should be fed. By plotting the amplitude of the excitation across the grid, we can learn the spatial distribution of the excitation.

The definition of the sparsity is the number of nonzero elements in a vector. A sparsest OPA configuration corresponds to the $\hat{\boldsymbol{w}}$ with the fewest nonzero entries. Therefore, identifying the zero entries is crucial. The result $\hat{\boldsymbol{w}}$ is a numerical solution that includes entries close to zero rather than exactly zero. Although entries close to zero can be treated as zeros, "close to zero" is a relative concept rather than an absolute threshold, making identifying zero entries challenging. The appropriate threshold level for distinguishing zeros from nonzeros depends on the maximum values and the distribution of entry amplitudes. Thus, a suitable method for separating and identifying zeros and nonzeros involves sorting the entries of $\hat{\boldsymbol{w}}$ in descending order and identifying the transition from nonzeros to close-zeros. Entries after this transition are considered close-zero and should be set to zero. This approach ties the sparsity of the results $\hat{\boldsymbol{w}}$ to the transition in the sorted amplitude distribution of $\hat{\boldsymbol{w}}$.

The excitation vector $\hat{\boldsymbol{w}}$ generates the corresponding beampattern, denoted by $\hat{\boldsymbol{p}} = \boldsymbol{S}\hat{\boldsymbol{w}}$. This pattern is the focus of our analysis regarding the beampattern characteristics. The beampattern is examined in terms of beamwidth, peak sidelobe level, and peak to sidelobe level ratio (PSR).

Based on the above reasoning, the results are analyzed from three perspectives:

- The performance of the beampattern, $\hat{\boldsymbol{p}}$, in terms of beamwidth, peak sidelobe level and PSR.
- The amplitude spatial distribution of the $\hat{\boldsymbol{w}}$ over the grid.
- The distribution of the amplitude of $\hat{\boldsymbol{w}}$ sorted in a descending order

The first aspect is in the pattern domain, meaning it involves the analysis of beampattern performance. The last two aspects relate to the excitation domain: the second aspect aids in analyzing the geometrical distribution of the excitation power, while the third aspect reveals the sparsity of the resulting excitation vector $\hat{\boldsymbol{w}}$.

3.3 Results of LASSO

This section presents the results obtained by solving the LASSO problem (2.8) using various values for the hyperparameter ϵ. This ϵ can be interpreted as the permissible

matching error between the generated and desired patterns. According to the geometrical interpretation shown in Fig.2.2a, the meaningful range for ϵ is determined by the least square solution and the solution where all entries are zero.

The least square solution is given by $\hat{\boldsymbol{w}}_{LS} = \boldsymbol{S}^{\dagger}\boldsymbol{p}_d$, where the $\boldsymbol{S}^{\dagger}$ is the pseudo-inverse of matrix $\boldsymbol{S}$. Conceptually, obtaining this least square solution is equivalent to solving the optimization problem:

$$\hat{\boldsymbol{w}}_{LS} = \arg\min_{\boldsymbol{w}} \|\boldsymbol{S}\boldsymbol{w} - \boldsymbol{p}_d\|_2 \tag{3.2}$$

The matching error ϵ_{LS} corresponding to $\hat{\boldsymbol{w}}_{LS}$ serves as the lower bound of the range for ϵ. This is a feasible bound since values below this bound are infeasible. However, the pseudo-inverse approach failed to deliver a solution due to the large condition number of matrix $\boldsymbol{S}$, causing numerical issues. Therefore, the optimization approach was used to determine the ϵ_{LS}. The zero solution $\hat{\boldsymbol{w}} = \boldsymbol{0}$ provides the upper bound for ϵ. The problem (2.8) aims to minimize $\|\boldsymbol{w}\|_1$, shrinking the l_1-norm ball in $\mathbb{C}^N$. The minimum achievable value of $\|\boldsymbol{w}\|_1$ is 0, corresponding to a zero vector. This zero vector results in a matching error ϵ_{max} that only depends on the desired pattern and its samplings.

Increasing the ϵ allows the l_1-norm ball shrink further, resulting in a decreased $\|\hat{\boldsymbol{w}}\|_1$ value. The solutions of solving the LASSO problem (2.8) at two boundary conditions are known: one with all zeros and another with excitation distribution as shown in Fig.3.1. Based on these two results, the expectation is that increasing ϵ between two boundary values will progressively reduce the sparsity in $\hat{\boldsymbol{w}}$.

A series ϵ values were unevenly selected from the $[\epsilon_{LS}, \epsilon_{max}]$. These values of ϵ are depicted in Fig.3.2a. The $\|\hat{\boldsymbol{w}}\|_1$ values obtained by solving problem (2.8) with these ϵ are illustrated in Fig3.2b. The $\|\hat{\boldsymbol{w}}\|_1$ exhibits three almost linearly decreasing stages with distinct slopes on a logarithmic scale. This decrease in $\|\hat{\boldsymbol{w}}\|_1$ aligns with the geometrical interpretation; a larger ϵ permits greater relaxation for the matching constraint and further shrinkage of the l_1-norm ball, leading to a smaller $\|\hat{\boldsymbol{w}}\|_1$. This summarizes the high-level impact of the ϵ on solving the LASSO problem (2.8). A more detailed examination of the LASSO problem results will be presented below. For simplicity, only selected typical results will be discussed.

Firstly, the results are analyzed in terms of beampattern, represented as $\hat{\boldsymbol{p}} = \boldsymbol{S}\hat{\boldsymbol{w}}$. Beampatterns for different values of ϵ are shown in Fig.3.3. From the plot, it is evident that all beampatterns exhibit a similar pencil-beam shape. Given that the intensity is represented on a logarithmic scale, the sidelobe regions at both ends can effectively be considered zero, despite the graphical differences. Thus, the most notable distinction among these beampatterns lies within the mainlobe. It is observed that beampatterns associated with larger ϵ values present a lower peak at the mainlobe. From this, it can be concluded that the matching diminishes as ϵ increases. This observation aligns with expectations, given that ϵ serves as a direct control mechanism over the match between the generated and the desired patterns through the constraint $\|\boldsymbol{S}\boldsymbol{w} - \boldsymbol{p}_d\|_2 \leq \epsilon$ in (2.8).

Due to the form of the constraint $\|\boldsymbol{S}\boldsymbol{w} - \boldsymbol{p}_d\|_2 \leq \epsilon$, it is logical to associate ϵ with the concept of mean square error (MSE), which is the average of the squares of the differences between the desired and generated patterns. Ideally, if the matching error represented by ϵ were evenly distributed across all sampling points, this error could be interpreted as noise. Linking ϵ to the noise level via MSE would enhance the

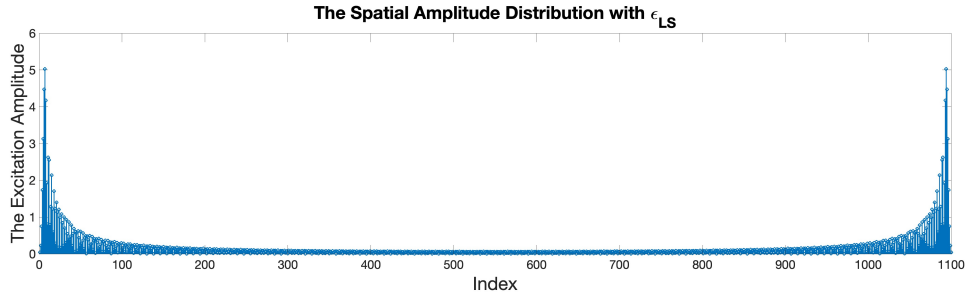

(a) The spatial distribution of the least square solution $\hat{\boldsymbol{w}}_{LS}$.

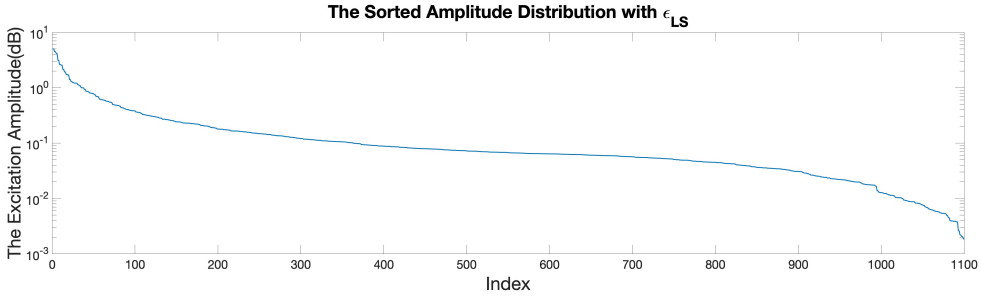

(b) The sorted amplitude distribution of the least square solution $\hat{\boldsymbol{w}}_{LS}$.

Figure 3.1: The solution of solving least square problem (3.2). As shown in (a), the most excitation power is allocated at two ends of the grid. There is very little power is distributed at the centre of the grid. Although there are many small entries, the least square solution has no clear transition in the sorted amplitude distribution (b). The least square solution does not promote sparsity in the solution.

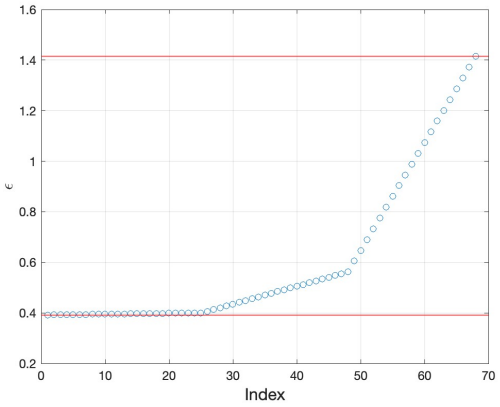

(a) The values of ϵ used for simulation

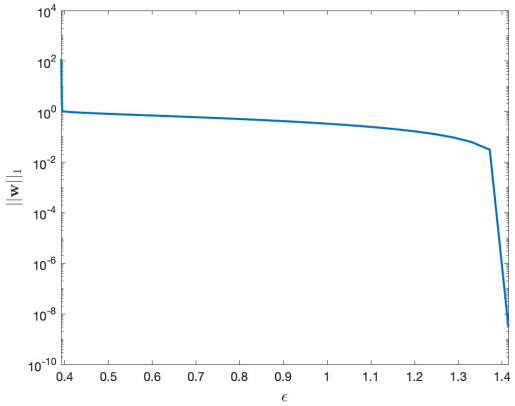

(b) The resulting l_1-norm vs ϵ

Figure 3.2: The series of simulations with different ϵ as in (a) and the results l_1-norm of the excitation vector in (b). As shown in (b), the l_1-norm decreases rapidly when ϵ is around the lower bound. It also reaches zero at ϵ_{max}. The variation in the middle is nearly linear in the log scale.

interpretability of the algorithm, aiding users in designing optimal OPA configurations.

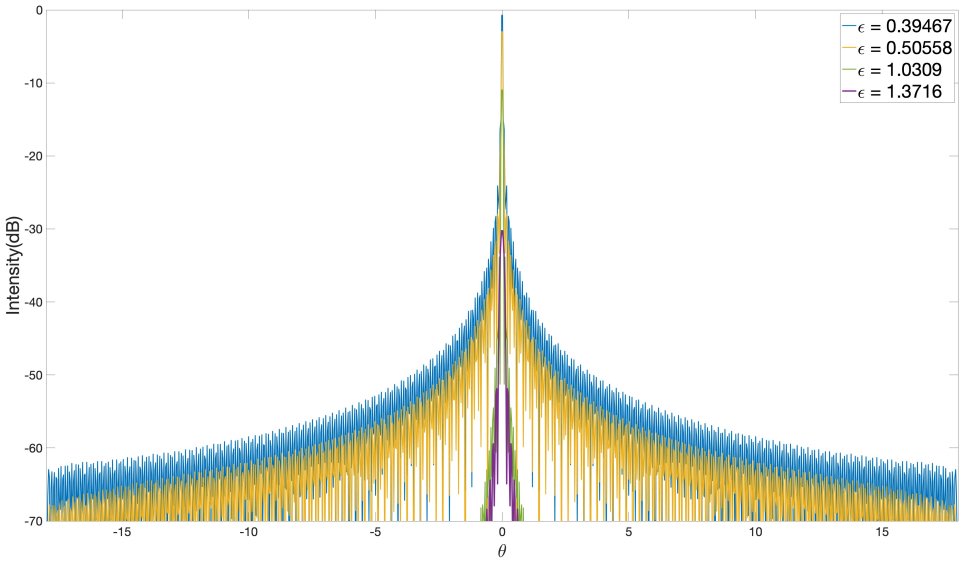

Figure 3.3: The generated beampattern with increasing ϵ. The most significant difference is at the mainlobe region.

However, if ϵ serves merely as an aggregate indicator of beampattern matching, its utility is more limited. Unfortunately, the following analysis of how beampatterns evolve with increasing ϵ reveals that the most pronounced changes occur within the mainlobe. This observation undermines the idea of interpreting ϵ directly as noise affecting the generated pattern, suggesting that the matching error is not uniformly distributed across the beampattern. This realization indicates that while ϵ is a valuable parameter for controlling the overall fit between the desired and generated patterns, it may not offer a straightforward correlation with noise in the way one might hope for enhancing algorithm interpretability.

The expression of the beampattern matching constraint is given by:

$$\|\boldsymbol{S}\boldsymbol{w} - \boldsymbol{p}_d\|_2 = \sqrt{\sum_{l=1}^{L} (\boldsymbol{s}^H(\theta_l)\boldsymbol{w} - p_d(\theta_l))^2} \leq \epsilon \tag{3.3}$$

where ϵ^2 can be interpreted as the maximum power of the 'noise'. This interpretation suggests that as ϵ changes, the value of ϵ^2 represents a cap on the total deviation between the desired and the generated beampatterns across all sampling points. For meaningful comparison across different values of ϵ, it's necessary to normalize ϵ^2 to unit power. This normalization process ensures that comparisons of the deviations at different sampling points are made on a consistent basis, regardless of the total deviation specified by ϵ. After normalization, the term $(\boldsymbol{s}^H(\theta_l)\boldsymbol{w} - p_d(\theta_l))^2$ represents the fraction of the total deviation (expressed as a percentage of ϵ^2) that is attributed to the sampling point θ_l.

The distribution of normalized squared matching error, as illustrated in Fig.3.4,

provides insight into how the allowable deviation is allocated across the beampattern. This detailed examination reveals that treating ϵ directly as a representation of noise on the beampattern might be overly simplistic. The distribution of squared errors suggests that deviations from the desired pattern are not uniformly distributed as one might expect from traditional noise. Instead, these deviations are influenced by the specific values of ϵ and how the optimization algorithm allocates the allowable deviation across different parts of the beampattern, particularly affecting areas like the mainlobe and sidelobes differently. This nuanced understanding underscores the complexity of interpreting ϵ solely as noise and highlights the importance of considering how deviations are distributed across the beampattern when using ϵ to guide the design of OPA configurations.

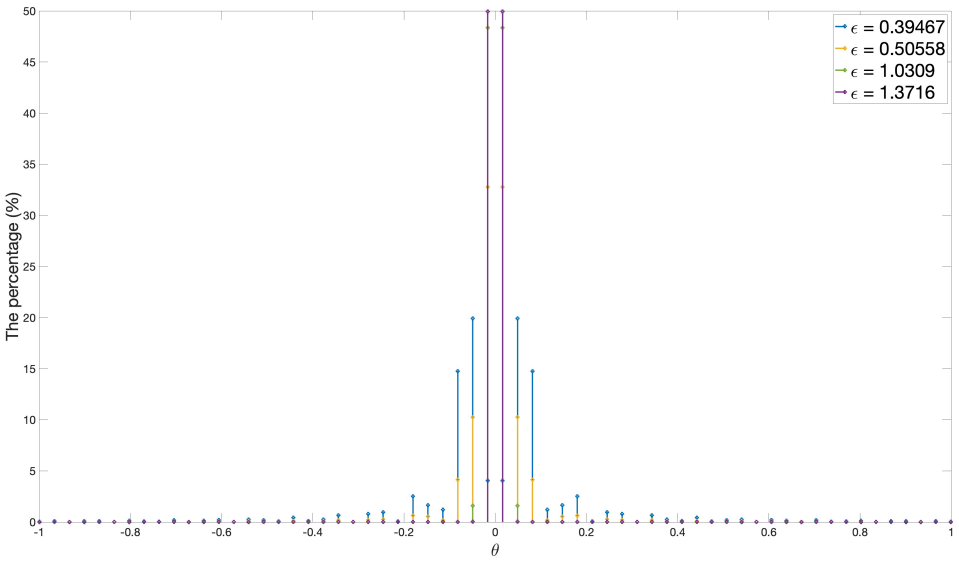

Figure 3.4: The percentage of the squared matching error (ϵ^2) distribution over the beampattern. The most amount of ϵ^2 is around the mainlobe regardless of the value of ϵ. There is clearly a trend of increasing ϵ gathering the matching error to the mainlobe. There is a significant error outside the mainlobe for the small ϵ. For the largest ϵ in the figure, all error is on the two sampling points at the mainlobe.

The impact of increasing ϵ on the resulting beampattern is clear and consistent: increasing ϵ reduces the peak of the mainlobe and concentrates the matching error within the mainlobe. However, the evolution of the results, in terms of $\hat{\boldsymbol{w}}$, demonstrates inconsistency. The amplitude spatial distribution, as shown in Fig.3.5a reveals that as ϵ increases from its lower bound, the excitations at both ends decrease, whereas the excitations in the middle increase. This phenomenon is evident when comparing the blue plot in Fig.3.5a with Fig.3.1a. With an increase in ϵ, $\hat{\boldsymbol{w}}$ evolves towards the solution marked in yellow. This process significantly diminishes the excitations at both ends. In the yellow solution, smaller excitations are interspersed among larger ones, resulting in a pronounced variation in amplitude along the grid. The larger excitations

create an envelope. Continuing to increase ϵ shifts the solution towards the one in green, flattening the excitation envelope and minimizing variation across the grid. A visual inspection of the green plot in Fig.3.5a suggests that this configuration might possess the most active elements. This conclusion is further supported by Fig.3.5b. Subsequently increasing ϵ reduces the excitations to zero from the grid's ends until all entries reach zero, as depicted by the solution in purple.

The evolution of $\hat{\boldsymbol{w}}$ in terms of spatial distribution unfolds in three stages, yet no obvious pattern emerges regarding the sparsity of the solutions. Defining sparsity as the transition location in the sorted amplitude distribution reveals that the solution in blue offers an OPA configuration even sparser than the one in green. This observation underscores that compromising on the beampattern quality does not necessarily lead to an enhancement in sparsity. Given these findings and the accompanying analysis, it is evident that the LASSO formulation fails to yield the sparsest OPA design that meets the specified beampattern criteria.

ϵ	Peak Mainlobe	Peak Sidelobe	PSR	$\|\hat{\boldsymbol{w}}\|_1$	$\|\hat{\boldsymbol{w}}\|_2$	Beamwidth
0.3947	0.5240	-16.2664	16.7904	1.0963	0.0501	0.05
0.5056	-1.7914	-19.7477	17.9563	0.8136	0.0371	0.05
1.0309	-10.2197	-32.0383	21.8186	0.3083	0.0106	0.06
1.3716	-30.0856	-51.4833	21.3977	0.0313	0.0016	0.14

Table 3.1: The quantified beampattern characteristics of the results of solving LASSO problem.

Table 3.1 presents a summary of the characteristics of results. This examination use a highly refined sampling resolution, $L = 200001$, to ensure detailed accuracy in beamwidth and sidelobe characteristics. Such a large L aims to secure a precise measurements, particularly of the mainlobe beamwidth. The odd value of L guarantees that the beampattern's peak is directly sampled, thus enabling accurate peak level assessments. Based on the previous results and the associated analysis, we can conclude that this LASSO formulation fails to deliver the sparsest OPA design with the given beampattern requirements.

3.4 Results of Thresholding

The previous section presents the results of solving the LASSO problem (2.8). According to the results and analysis in the previous section, we concluded that this formulation fails to achieve the objective of finding the sparest OPA configuration that meets automotive requirements. This section demonstrates the results of applying the thresholding algorithm to the solutions obtained problem (2.8).

As explained in Section 2.2.2, the thresholding operation acts on the excitation vector $\hat{\boldsymbol{w}}$. It retains the k largest entries of $\hat{\boldsymbol{w}}$ and sets the remaining entries to zero, resulting in a new excitation vector denoted by $\hat{\boldsymbol{w}}_k$. This method ensures an excitation vector $\hat{\boldsymbol{w}}_k$ with exactly k nonzero entries, representing an OPA configuration with k active elements. Although determining the optimal choice for k remains a challenge, thresholding provides a means to generate a sparse excitation and, consequently, a

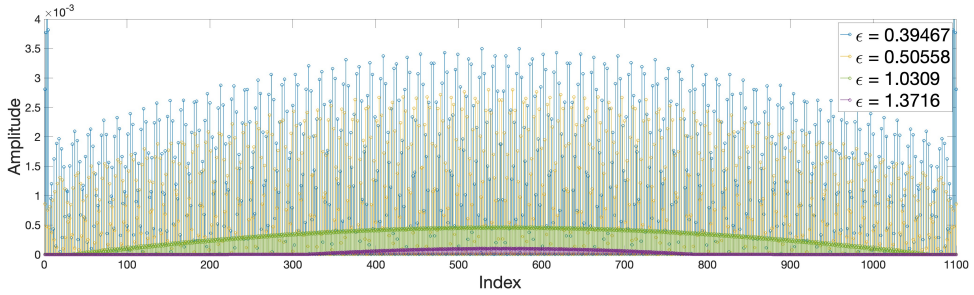

(a) The amplitude distribution of $\hat{\boldsymbol{w}}$ over the grid.

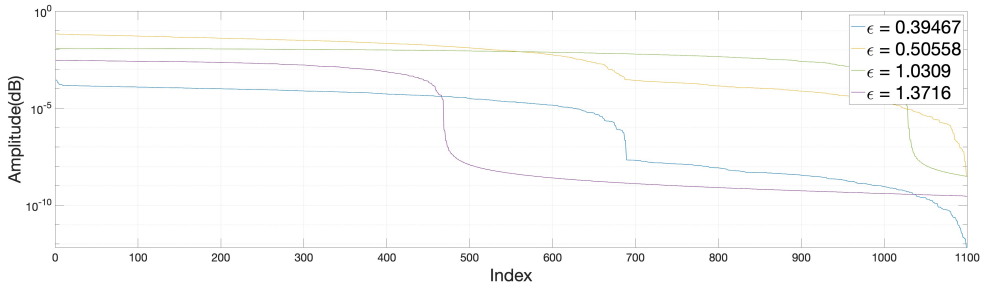

(b) The sorted amplitude distribution of $\hat{\boldsymbol{w}}$.

Figure 3.5: The results $\hat{\boldsymbol{w}}$ in terms of spatial distribution (a) and the amplitude distribution sorted in descending order (b). The spatial distribution of $\hat{\boldsymbol{w}}$ has multiple forms. The evolution is from one form to another along the increasing ϵ. The sorted amplitude distribution shows the transition in amplitude. No pattern is found in the transition behaviour along the increasing ϵ.

sparse OPA configuration. Thresholding introduces errors in the excitation vector, quantified by the error vector:

$$\boldsymbol{e}_w = \hat{\boldsymbol{w}} - \hat{\boldsymbol{w}}_k \tag{3.4}$$

which contains the entries that have been set to zero.

An instance demonstrating impact of thresholding is presented in Fig.3.6, using the solution $\hat{\boldsymbol{w}}$ at $\epsilon = 0.50558$ from the previous section (depicted in yellow in Fig.3.3). The range of feasible k values is the set of integers between $[0, 1100]$. When $k = 1100$, it signifies the original solution without thresholding. For simplicity of demonstration, only three selected values of k and their corresponding excitations and beampatterns are discussed. The difference between the original excitation vector and the post-thresholding excitations are shown in Fig.3.6, illustrating the error introduced by thresholding at different k values. Since thresholding consider only amplitude, the locations of these errors on the grid depend on the original spatial distribution of $\hat{\boldsymbol{w}}$, i.e., the smaller values in $\hat{\boldsymbol{w}}$ are set to zero first. Regardless of where the zeroed entries in $\hat{\boldsymbol{w}}$ are located, the thresholding algorithm consistently delivers a sparser solution by reducing k.

The k-sparse excitation generates a beampattern $\hat{\boldsymbol{p}}_k = \boldsymbol{S}\hat{\boldsymbol{w}}_k$. The corresponding beampatterns are shown in Fig.3.7. The error introduced in the excitation vector $\hat{\boldsymbol{w}}$ affects the generated beampattern through $\hat{\boldsymbol{p}} = \boldsymbol{S}\hat{\boldsymbol{w}}$. Two distinct impacts of thresholding are observed: first, the peak of the mainlobe decreases with a decrease in k; second,

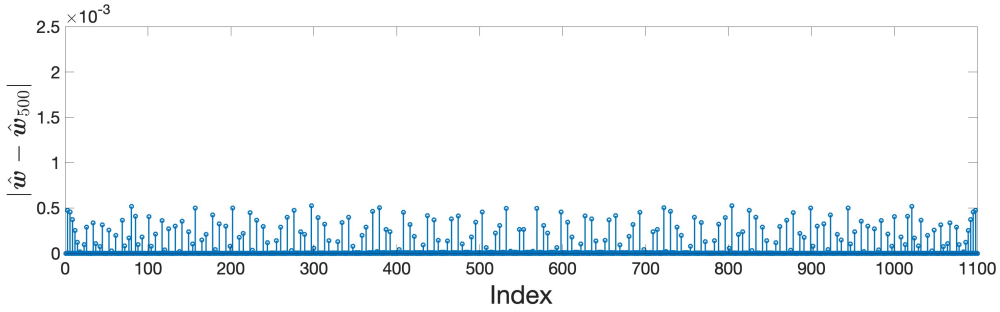

(a) The error introduced in excitation vector when $k = 500$

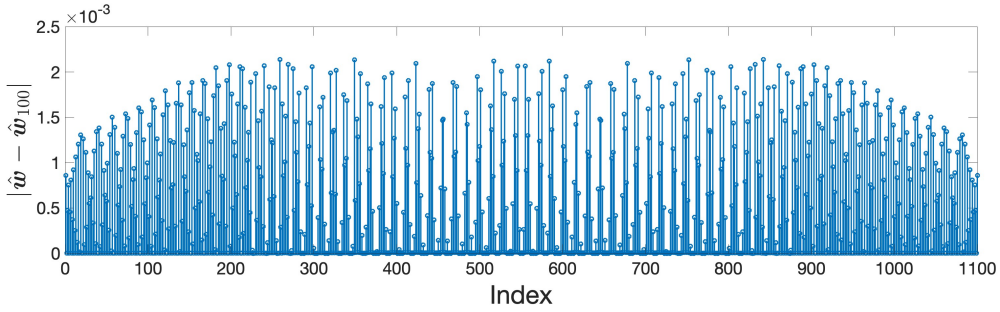

(b) The error introduced in excitation vector when $k = 100$

Figure 3.6: The error introduced in $\hat{\boldsymbol{w}}_k$ by thresholding the excitation vector to k sparse. The nonzero entries in these plot are the entries that have been forced to zero.

the beampattern becomes immersed in a noise-like floor. Comparing beampatterns for $k = 1100$ and 500, the peak is reduced, and the sidelobe region is elevated, creating a nearly uniform noise floor. However, the error introduced in the beampattern is not perfectly uniformly distributed. For $k = 500$, spikes emerge around $\pm 15°$, becoming more notable as k is further reduced to 100, as shown in Fig.3.7, where additional spikes appear $\pm 5°$.

These observations indicate that thresholding the excitation vector $\hat{\boldsymbol{w}}$ introduces a noise-like error on the beampattern. To substantiate this claim, the differences between the beampatterns $|\hat{\boldsymbol{p}} - \hat{\boldsymbol{p}}_k|$ are depicted in Fig.3.8, showing the error spread across the beampattern. The yellow horizontal line represents the mean of $|\hat{\boldsymbol{p}} - \hat{\boldsymbol{p}}_k|$, further proving that thresholding spreads the error in the beampattern.

Denoting the $\boldsymbol{e}_p = \hat{\boldsymbol{p}} - \hat{\boldsymbol{p}}_k \in \mathbb{C}^L$ and $\boldsymbol{e}_w = \hat{\boldsymbol{w}} - \hat{\boldsymbol{w}}_k \in \mathbb{C}^N$, the relationship between $\boldsymbol{e}_p$ and $\boldsymbol{e}_w$ is given by:

$$\boldsymbol{e}_p = \boldsymbol{S}\boldsymbol{e}_w \tag{3.5}$$

The power of the error in beampattern can be expressed as:

$$\begin{aligned} \boldsymbol{e}_p^H \boldsymbol{e}_p =& (\boldsymbol{S}\boldsymbol{e}_w)^H \boldsymbol{S}\boldsymbol{e}_w \\ =& \boldsymbol{e}_w^H \boldsymbol{S}^H \boldsymbol{S}\boldsymbol{e}_w \end{aligned} \tag{3.6}$$

The characteristic of matrix $\boldsymbol{S}^H\boldsymbol{S}$ is pivotal in determining the power of error in the beampattern. (In this project, as the excitations are distributed in space rather than time, the excitations are measured in power rather than energy.) As shown in Fig.3.9,

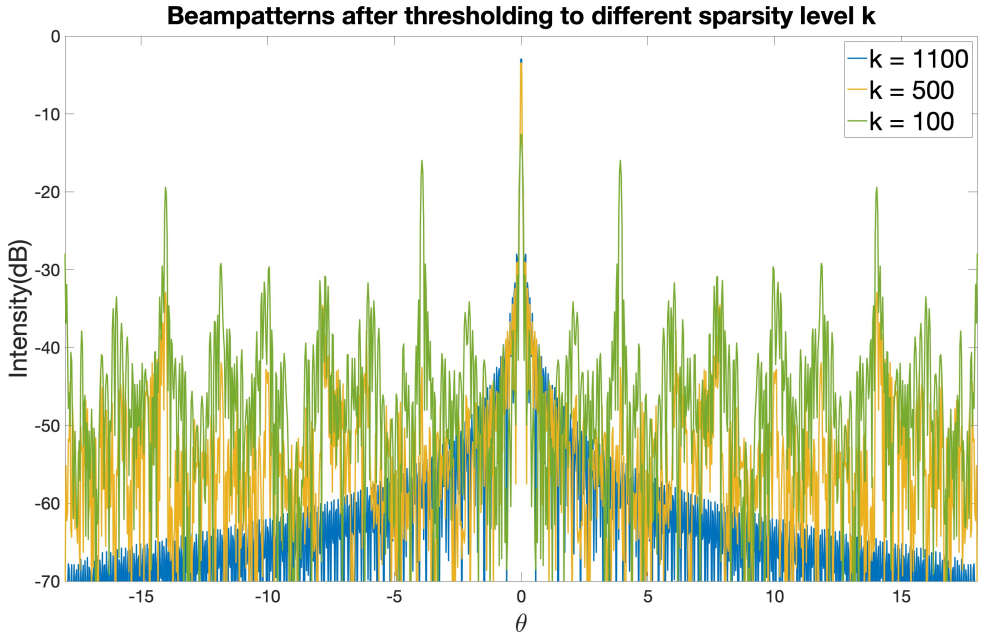

Figure 3.7: Beampatterns of thresholding the excitation vector at different k

the matrix $\boldsymbol{S}^H\boldsymbol{S}$ closely resembles an identity matrix scaled by $L = 1100$, allowing equation (3.6) to be approximated as:

$$\|\boldsymbol{e}_p\|_2^2 \approx L\|\boldsymbol{e}_w\|_2^2 \tag{3.7}$$

where $\|\boldsymbol{e}_p\|_2^2 = \boldsymbol{e}_p^H\boldsymbol{e}_p$ and $\|\boldsymbol{e}_w\|_2^2 = \boldsymbol{e}_w^H\boldsymbol{e}_w$. This equation establishes a power relationship between the error in the excitation and the error in the beampattern, suggesting that $\boldsymbol{S}^H\boldsymbol{S} \approx L\boldsymbol{I}$.

The $\|\boldsymbol{e}_p\|_2^2$ can also be expressed as

$$\begin{aligned}\|\boldsymbol{e}_p\|_2^2 =& \|\hat{\boldsymbol{p}} - \hat{\boldsymbol{p}}_k\|_2^2 \\ =& \sum_{l=1}^{L} |p_l - p_{k,l}|^2 \\ \approx& L\|\boldsymbol{e}_w\|_2^2\end{aligned} \tag{3.8}$$

This expression can be further interpreted in terms of the root mean square error (RMSE), which measures the average amplitude deviation of the entries in vector $\hat{\boldsymbol{p}}_k$ from corresponding entries in vector $\hat{\boldsymbol{p}}$. The average deviation in p is given by $\bar{e}_p = \sqrt{\frac{L\|\boldsymbol{e}_w\|_2^2}{L}} = \|\boldsymbol{e}_w\|_2$. Since the sidelobe region for beampattern generated by $\hat{\boldsymbol{w}}$ is predominantly zero, the noise floor in the sidelobe region can be expected to be approximately $\|\boldsymbol{e}_w\|_2$. This interpretation directly relates the error in the excitation vector to the observed error in the beampattern, providing a guideline for selecting the smallest k for a given excitation vector $\hat{\boldsymbol{w}}$ and an acceptable peak sidelobe level. Table 3.2 summarizes the characteristics of the thresholding results. This examination uses a number of samplings $L = 200001$.

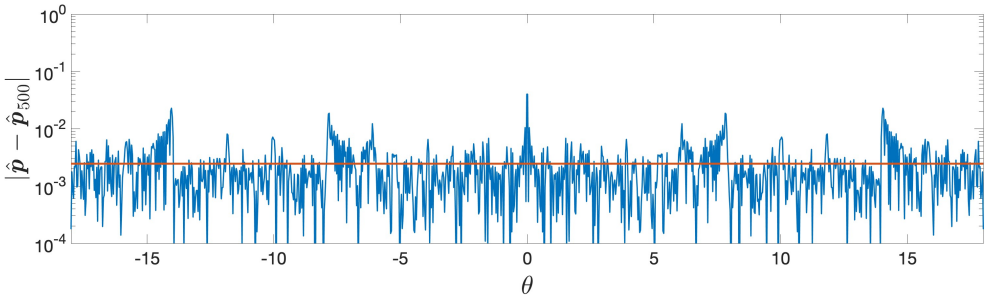

(a) The error distribution of the beampattern when $k = 500$

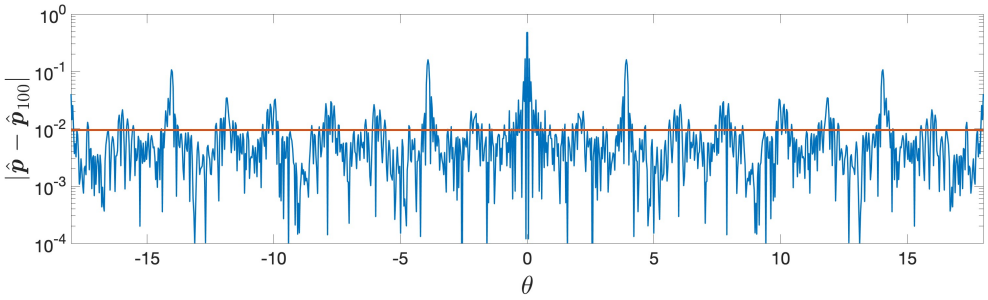

(b) The error distribution of the beampattern when $k = 100$

Figure 3.8: The plot of power difference between original beampattern ($\boldsymbol{p}$) and beampattern after thresholding ($\boldsymbol{p}_k$). (a) $k = 500$. (b) $k = 100$. The horizontal line in yellow indicates the mean of all differences across the beampattern.

k	Peak Mainlobe	Peak Sidelobe	PSR	$\|\hat{\boldsymbol{w}}_k\|_1$	$\|\hat{\boldsymbol{w}}_k\|_2$	Beamwidth
1100	-1.7914	-19.7477	17.9563	0.8136	0.0371	0.05
600	-2.3230	-20.6874	18.3644	0.7653	0.0369	0.05
100	-12.2631	-15.9424	3.6793	0.2437	0.0244	0.09

Table 3.2: The quantified beampattern characteristics of the results of thresholding the results.

However, due to the presence of spikes as illustrated in Fig.3.7, this approach only offers a coarse guideline for determining the optimal k based on specific performance metrics. While a direct analytical relationship between the spikes and the thresholding level k is not readily available, conducting an exhaustive search for k values can identify the smallest k that leads to a beampattern with a peak sidelobe level that meets acceptable standards. Since the requirement for beamwidth can be addressed by solving the LASSO problem (2.8), combining the LASSO formulation with thresholding effectively achieves the goal of identifying the sparest OPA configuration that satisfies automotive requirements.

3.5 Results of Enhancing Sparsity via Reweighted l_1-norm

The previous section demonstrated the effectiveness of thresholding in promoting sparsity within the excitation vector $\hat{\boldsymbol{w}}$, utilizing the results of the LASSO problem (2.8) as

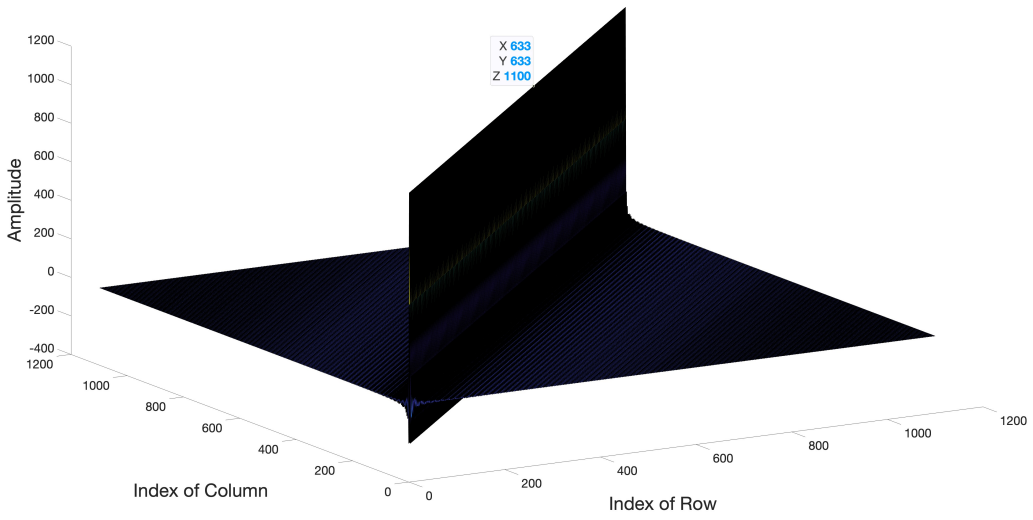

Figure 3.9: The plot of the real part of matrix $\boldsymbol{S}^H\boldsymbol{S}$. The diagonal entries are all 1100 (L). Therefore, the matrix is almost an identity matrix multiplied by scale 1100 (L).

input. Thresholding compensates for the LASSO problem's shortcomings in controlling of the level of sparsity. An alternative approach involves enhancing the sparsity at the stage of solving problem (2.8) itself. As discussed in Section 2.2.3, the difference between the l_0-norm in (2.7) and its l_1-norm approximation in (2.8) is significant. Relying on the l_1-norm as an approximation to solve for the original problem is not always dependable. Employing the iterative algorithm (1), the reweighted l_1-norm more closely approximates the l_0-norm, enhancing sparsity.

The convergence of the algorithm, for varying values of ϵ, is depicted in Fig.3.10. Initially, the optimization process is equivalent to standard l_1-norm minimization, where the objective function is simply the sum of the absolute values of all entries in $\boldsymbol{w}$. The impact of applying a weighted l_1-norm becomes evident from the second iteration onwards, transforming the objective function into a weighted sum of the a weighted sum of absolute values of all entries. This adjustment makes the weighted l_1-norm behave more closely to the l_0-norm, which quantifies the number of nonzero entries. As a result, an increase in $\|\boldsymbol{\Gamma}^{(m)}\boldsymbol{w}\|_1$ is observed from the first to the second iteration for every ϵ value. Subsequent to the second iteration, the optimal value of the objective function demonstrates a consistent decrease with each iteration, indicating that the algorithm achieves convergence.

An example illustrating the convergence and the impact of reweighted l_1-norm minimization is presented in Fig.3.11. This figure displays the distributions of excitation vector at each iteration when solving the LASSO problem iteratively with $\epsilon = 0.50558$. The initial result, depicted by the blue line from Section 3.3, shows a notable change at the next iteration (the orange line), where a sharp transition in the sorted amplitude distribution becomes evident. This sharp transition continues to evolve towards

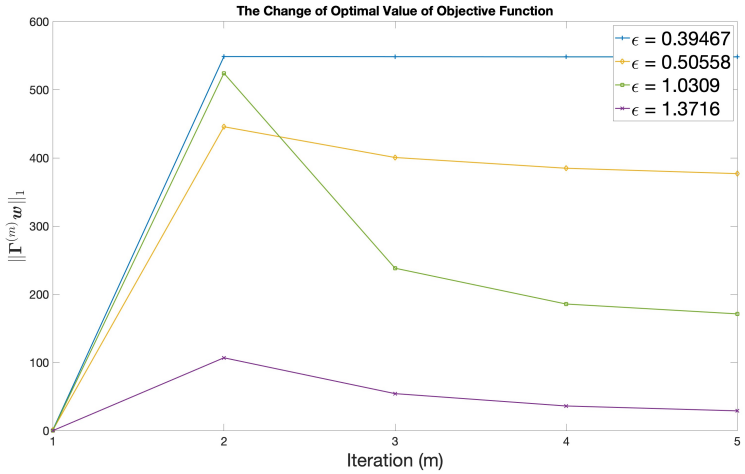

Figure 3.10: The optimal value of the objective function at each iterations when ϵ takes different values. The increase in the value of $\|\mathbf{\Gamma}^{(m)}\boldsymbol{w}\|_1$ from the first to the second iteration is due to the weighting of l_1-norm. The convergence starts from the second iteration.

convergence in subsequent iterations, a behavior consistent across any ϵ value.

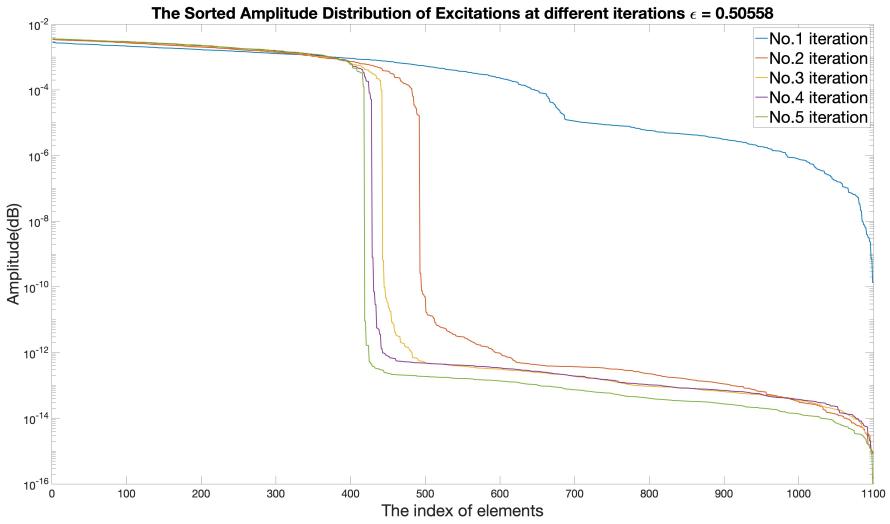

Figure 3.11: The curves of sorted amplitude distribution. The results converge with iterations.

These iterations also affect the beampattern. Fig.3.12 compares the beampatterns from the first iteration to those after convergence, revealing a noise floor similar to that introduced by the thresholding algorithm. Thus, iterative reweighted l_1-norm minimization effectively elevates the sidelobe region in the beampattern in exchange for a reduced sparsity in excitation vector $\hat{\boldsymbol{w}}$.

For any given ϵ, the last iteration's solution is considered as the final one. When comparing the final solutions across different ϵ values, as shown in Fig3.13, the position

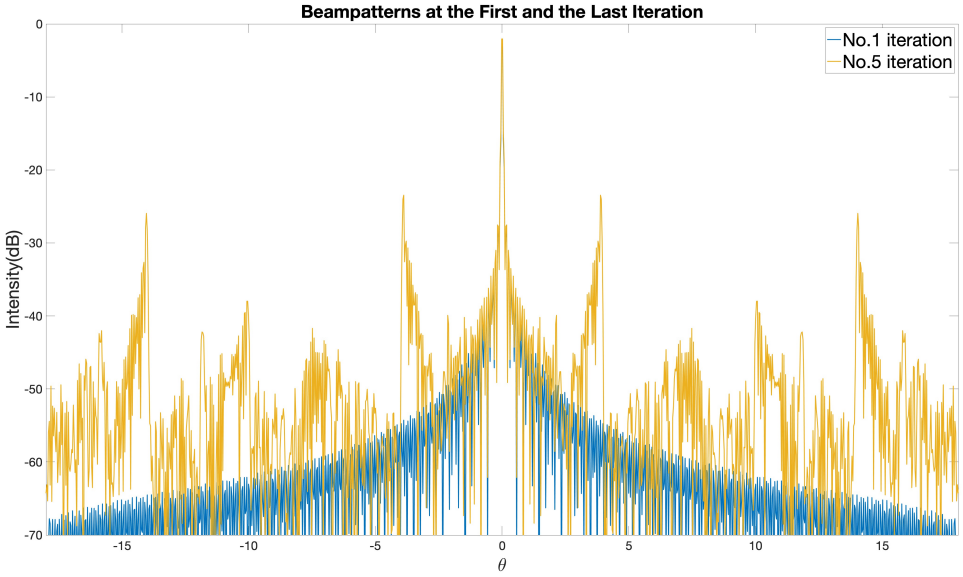

Figure 3.12: The beampatterns at the first and the last iteration. The difference is due to iterative reweighting the l_1-norm.

of the transition shifts leftward with increasing ϵ, directly impacting the sparsity of $\hat{\boldsymbol{w}}$. Unlike the results from the LASSO problem depicted in Fig.3.5b, which failed to establish a consistent relationship between sparsity and ϵ, the reweighted approach demonstrates a clear monotonic relationship. Fig.3.14 illustrates the spatial distribution of the resulting excitations, with a clear comparison made to the LASSO outcomes in Fig.3.5a, showcasing the sparsity enhancement. In terms of the beampattern, as depicted in Fig.3.15, an increasing ϵ correlates with a decrease in the peak sidelobe ratio (PSR). However, determining an ϵ value that achieves a specific PSR remains a challenge due to the absence of an analytical expression connecting ϵ and PSR. Thus, the empirical tuning of ϵ is necessary.

As illustrated in Fig.3.4, we conducted an analysis on how ϵ^2 is allocated in the deviations between the generated and desired patterns. The distribution of ϵ^2 under the reweighted l_1-norm minimization is depicted in Fig.3.16a. Comparing this figure with Fig.3.4 reveals the impact of iterative weighting on $\|\boldsymbol{w}\|_1$. Notably, for the same ϵ, reweighted l_1-norm minimization concentrates less error in the mainlobe. For instance, at $\epsilon = 0.50558$ (highlighted in yellow), the maximum percentage of ϵ^2 utilized at the two central sampling points decreases by more than 10%—from over 30% to under 20%. This reduction is accompanied by a dispersion of ϵ^2 on the remaining sampling points. This broader distribution is further evidenced in Fig.3.16b, where a significant portion of ϵ^2 is found near $\pm 4^\circ$ and $\pm 13^\circ$. The influence of reweighted l_1-norm minimization on the ϵ^2 distribution, as compared to normal l_1 minimization approach, remains consistent across various ϵ values.

Table 3.3 summarizes the characteristics of the reweighted l_1-norm minimization results. This examination is carried out with $L = 200001$. From these analyses and

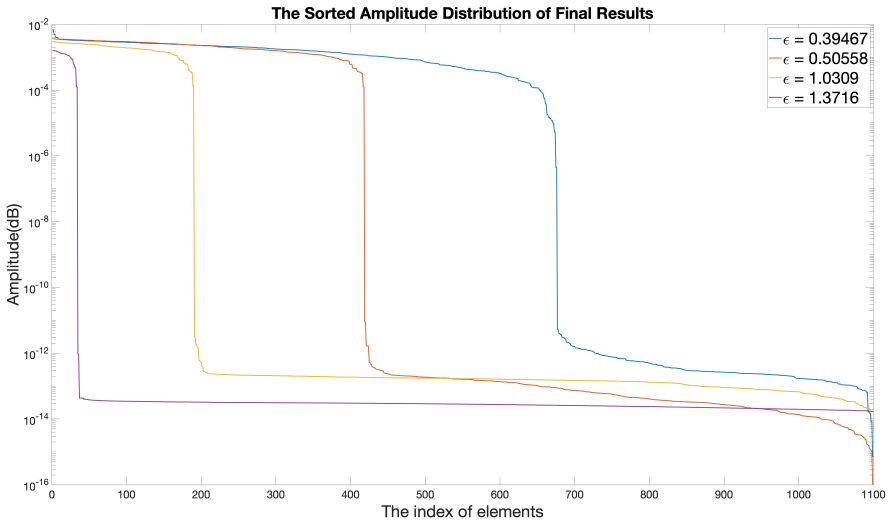

Figure 3.13: The sorted amplitude distribution of converged results when ϵ takes different values

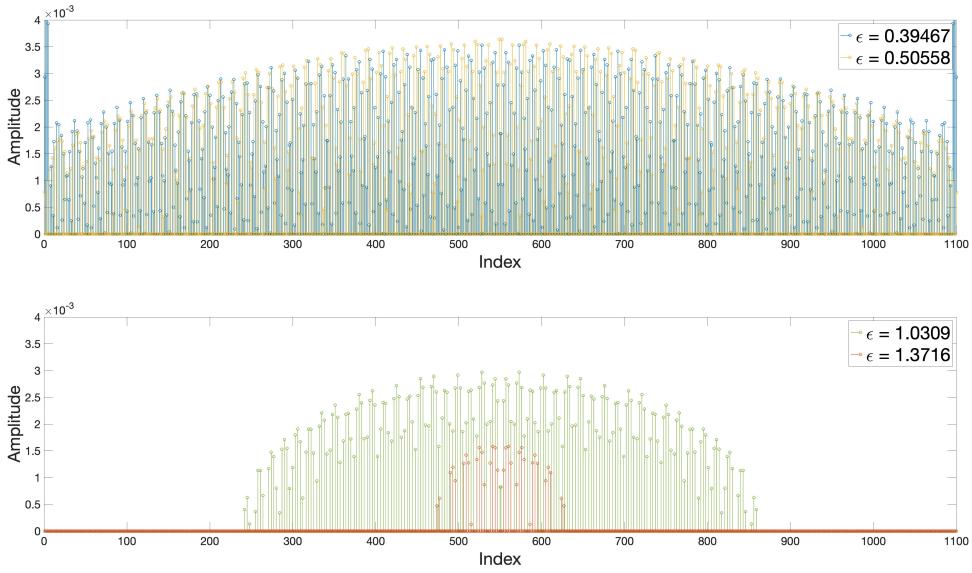

Figure 3.14: The spatial distribution of excitation with various ϵ

solutions, we can conclude that the reweighted approach is capable of meeting the objective: finding the sparsest OPA configuration that satisfies automotive requirements.

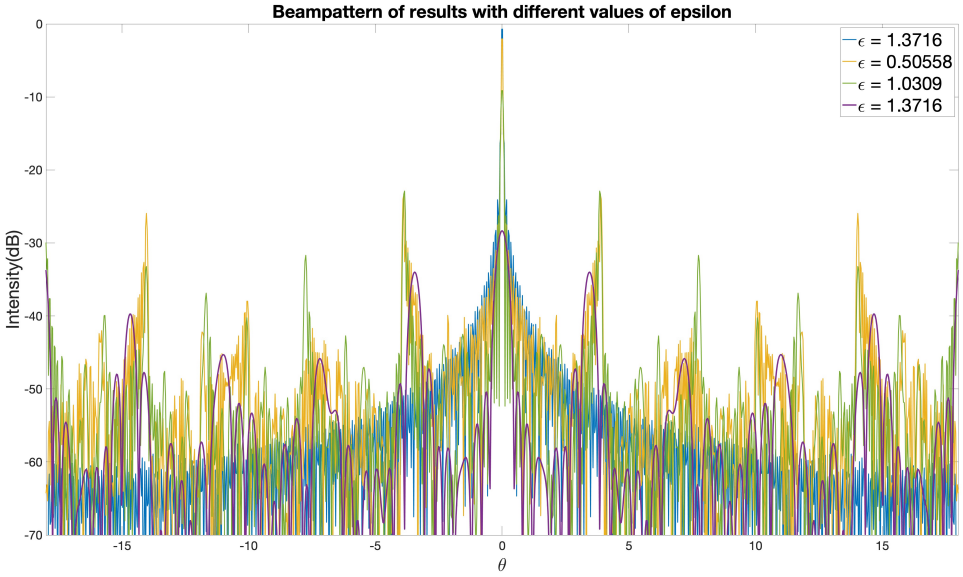

Figure 3.15: The beampatterns evolve with the increasing ϵ

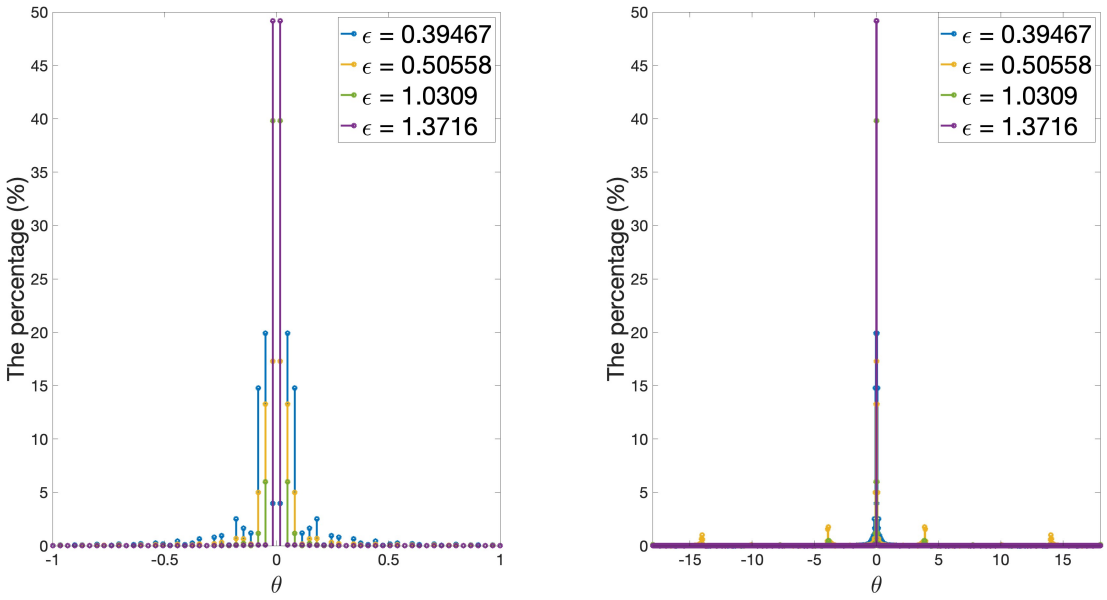

(a) The distribution of ϵ^2 around the mainlobe region.

(b) The distribution of ϵ^2 across the whole region of interest.

Figure 3.16: The percentage of the squared matching error (ϵ^2) distribution over the beampattern. Compared to LASSO problem, reweighted l_1-norm minimization concentrates less error in the mainlobe.

ϵ	Peak Mainlobe	Peak Sidelobe	PSR	$\|\hat{\boldsymbol{w}}\|_1$	$\|\hat{\boldsymbol{w}}\|_2$	Beamwidth	Sparsity
0.3947	0.5325	-16.2693	16.8018	1.1002	0.0505	0.050	676
0.5056	-0.8837	-18.9251	18.0414	0.9033	0.0477	0.052	418
1.0309	-8.7999	-22.6786	13.8787	0.3631	0.0279	0.096	190
1.3716	-28.3288	-33.9920	5.6632	0.0383	0.0070	0.391	34

Table 3.3: The quantified beampattern characteristics of the results of using the reweighted l_1-norm minimization.

Conclusions & Future Work

4

This project was dedicated to addressing the challenges associated with sparse OPA design, utilizing methodologies and techniques derived from the domains of compressive sensing and antenna design. This chapter summarizes the key findings and significant contributions of our work. Additionally, it outlines promising directions for future research and highlights compelling questions arising from this study.

4.1 Conclusions

This project begins by reviewing the background and motivations behind the development of sparse OPA. OPAs are considered to be the future of the LiDAR system and hold significant potential for automotive applications. These applications demand a LiDAR system capable of a detection range up to 200 meters and an angular resolution of 0.07 degrees. Given that the phase shifters in OPAs use heating to adjust the phase for each element, a uniformly spaced OPA necessitates a large number of elements to meet such stringent requirements, which leads to considerable power consumption and overheating issues. Sparse OPAs offer a solution by utilizing fewer elements, thereby addressing these concerns.

Designing a sparse OPA poses challenges, primarily because the position of elements is incorporated in the exponential term of the antenna array's beam pattern model. Consequently, most previous studies have applied evolutionary algorithms, such as genetic algorithms and particle swarm optimization. However, these algorithms are ineffective in identifying the minimum number of elements needed to satisfy given beam pattern requirements.

Focusing on a specific OPA architecture—linear OPA with amplitude control—we frame the design of the sparsest OPA to meet beampattern requirements within the sparse array synthesis framework. This methodology also accommodates another design constraint: the minimum spacing constraint, by utilizing a grid that represents the candidate positions for elements. Thus, the design process becomes a best subset selection problem.

In the realm of compressive sensing, a relaxed problem formulation substitutes the nonconvex l_0-norm with the convex l_1-norm, leading to the LASSO problem. As a convex problem, the LASSO problem can be efficiently solved using the CVX solver. However, the outcomes of the LASSO problem have not always aligned with expectations: while the resulting beampattern generally shows good performance, the resulting excitation vector does not consistently achieve the desired level of sparsity. The hyperparameter in the LASSO problem inadequately manages the trade-off between solution sparsity and the beampattern performance, and the difference between the generated and desired beampatterns is unevenly distributed across the matching range. This in-

consistency undermines the interpretation of hyperparameter as a mean square error in beampattern matching. Consequently, the LASSO problem formulation does not fully meet our research objectives.

An intuitive approach, thresholding, is then applied to achieve a sparse OPA configuration based on the LASSO solution. This method retains a given number of the largest entries to obtain a sparse solution. Thresholding the excitation vector significantly impacts the sidelobe region of the beampattern, raising the sidelobe levels similarly to introducing noise to the beampattern. Despite the success in correlating the error in the excitation vector with the noise floor in the beampattern, spikes significantly higher than the noise floor were observed. These spikes determine the peak sidelobe level, a critical performance metric for beampatterns. The strategy combines solving the LASSO problem to satisfy the beamwidth requirement, then applying thresholding until the peak sidelobe level attains a specified value. This approach effectively mitigates the limitation of the LASSO problem.

Lastly, a reweighted l_1-norm minimization is employed to enhance the sparsity of the solution. Since the LASSO problem leverages the l_1-norm as an approximation of l_0-norm, the intrinsic difference between these norms contributes to the failure of the LASSO approach. Iteratively reweighting l_1-norm provides a closer approximation to the l_0-norm. This method has proven effective in trading off the beampattern performance for the solution sparsity, producing a resulting beampattern with characteristics similar to thresholding effects (introducing a noise-like floor and spikes). Comparing solutions from the LASSO problem and the reweighted l_1-norm algorithm with identical ϵ values, the latter exhibits less concentration of matching error around the mainlobe due to spikes away from the mainlobe. In other words, this algorithm redistributes the allowable error (determined by ϵ) for the beampattern matching (represented by $\|\boldsymbol{S}\|_2$) compared to the LASSO problem. Nevertheless, the interpretation of the hyperparameter as a mean square error so that this hyperparameter can be related to the noise floor of the resulting beampattern is still impractical due to the presence of spikes. Since there's no analytical relation between the hyperparameter of the reweighted l_1-norm minimization and the peak sidelobe level, fine-tuning the hyperparameter is necessary to identify the sparsest OPA configuration with a specified peak sidelobe level.

4.2 Future Work

Several potential directions for future work have emerged throughout this project. Building on the analysis of the general sparse OPA design problem, as illustrated in Fig.1.12 and summarized in Table.1.1, future research could extend to developing algorithms for 2D OPAs, algorithms tailored for OPAs with only phase control, or delving into the exploration of off-grid algorithms that exploit the space between the grid points. Detailed discussions of each potential direction are presented below.

4.2.1 2D OPAs

The algorithm could be extended to accommodate 2D scenarios. 2D OPAs require distinct types of grating couplers, as detailed in [10]. Nevertheless, the mathematical

modelling of 2D arrays is a natural extension of the linear array model. The 2D problem's formulation is in the same form as (2.7) as presented in [33]. Therefore, the algorithms developed in this project are believed to be effective for 2D problems.

4.2.2 Uniform Amplitude Excitation

Given the reduced hardware complexity, OPA architectures without amplitude control remain favoured if the performance regarding the beampattern achieves an acceptable level. The absence of amplitude controllers, which require extra phase shifters, reduces both power consumption and wiring complexity. This challenge could be approached in two ways. Firstly, instead of optimizing against the excitations, a binary selection vector for elements with fixed phase shifts can be utilized. This selection vector can be relaxed into convex form and can be solved effectively [34, 35]. Consequently, the approach selects a subset of the ULA to match the desired beampattern without altering the amplitude of excitations. The second approach continues to optimize against the excitations, as in (2.8), but incorporates an additional constraint on the amplitude of excitations. Preliminary research on this topic suggests that managing such a constraint can be challenging, as the constraint of excitations with the same amplitude is non-convex. However, some inspiring works on waveform designs utilizing unimodular [36] and constant modulus algorithms exist. There is a paper that claims to be the first to address the problem of jointly optimizing the phase-only weight and antenna locations to achieve the desired transmit beampattern for phase-only array systems [37].

To our knowledge, we are the first to address the problem of jointly optimizing the phase-only (unimodular) waveform/weight and antenna locations to achieve desired transmit beampattern for colocated MIMO radar and phase-only array systems.

4.2.3 Off-Grid Algorithm

In addition to investigating algorithms tailored for various OPA architectures, exploring the potential of off-grid algorithms—which exploit the spaces between grid points—might further enhance the solution sparsity. In CS problems, the grid methods suffer from the mismatch of the grid points and the true parameters, namely the signal cannot be sparsely represented by the finite grid points when the true parameters fall between the grid points [38]. Off-grid algorithms have demonstrated superior performance in finding a sparse representation in such a scenario by exploiting the space between grid points.

Although there is no prior information about the "true" position in the sparse OPA scenario, it is reasonable to believe that the same improvement in sparse representation will also apply to sparse OPA design problems. After all, the sparse OPA design problem is essentially finding a sparse representation using the array factor model for a given beampattern. In other words, by exploiting the off-grid algorithm, the solution is potentially sparser. Two inspiring works addressing general array design challenges, [33, 39], serve as references for this exploration.

Bibliography

[1] Z. Dai, A. Wolf, P.-P. Ley, T. Glück, M. C. Sundermeier, and R. Lachmayer, "Requirements for automotive lidar systems," *Sensors*, vol. 22, no. 19, 2022.

[2] H. Hashemi, "A review of semiconductor-based monolithic optical phased array architectures," *IEEE Open Journal of the Solid-State Circuits Society*, vol. 1, pp. 222–234, 2021.

[3] E. J. Candès, M. B. Wakin, and S. P. Boyd, "Enhancing sparsity by reweighted l_1 minimization," *Journal of Fourier Analysis and Applications*, vol. 14, no. 5, pp. 877–905, 2008.

[4] C.-P. Hsu, B. Li, B. Solano-Rivas, A. R. Gohil, P. H. Chan, A. D. Moore, and V. Donzella, "A review and perspective on optical phased array for automotive lidar," *IEEE Journal of Selected Topics in Quantum Electronics*, vol. 27, no. 1, pp. 1–16, 2021.

[5] R. Roriz, J. Cabral, and T. Gomes, "Automotive lidar technology: A survey," *IEEE Transactions on Intelligent Transportation Systems*, vol. 23, no. 7, pp. 6282–6297, 2022.

[6] K. Żywanowski, A. Banaszczyk, and M. R. Nowicki, "Comparison of camera-based and 3d lidar-based place recognition across weather conditions," in *2020 16th International Conference on Control, Automation, Robotics and Vision (ICARCV)*, pp. 886–891, 2020.

[7] A. H. Lang, S. Vora, H. Caesar, L. Zhou, J. Yang, and O. Beijbom, "Pointpillars: Fast encoders for object detection from point clouds," in *2019 IEEE/CVF Conference on Computer Vision and Pattern Recognition (CVPR)*, pp. 12689–12697, 2019.

[8] Y. Li and J. Ibanez-Guzman, "Lidar for autonomous driving: The principles, challenges, and trends for automotive lidar and perception systems," *IEEE Signal Processing Magazine*, vol. 37, no. 4, pp. 50–61, 2020.

[9] T. Raj, F. H. Hashim, A. B. Huddin, M. F. Ibrahim, and A. Hussain, "A survey on lidar scanning mechanisms," *Electronics*, vol. 9, no. 5, 2020.

[10] R. Fatemi, A. Khachaturian, and A. Hajimiri, "A nonuniform sparse 2-d large-fov optical phased array with a low-power pwm drive," *IEEE Journal of Solid-State Circuits*, vol. 54, no. 5, pp. 1200–1215, 2019.

[11] J. Wang, W. Cheng, W. Zhu, M. Lu, Y. Chen, S. Shi, C. Guo, G. Hu, Y. Cui, and B. Yun, "Optimization and comprehensive comparison of thermo-optic phase shifter with folded waveguide on sin and soi platforms," *Optics Communications*, vol. 555, p. 130242, 2024.

[12] J. He, T. Dong, and Y. Xu, "Review of photonic integrated optical phased arrays for space optical communication," *IEEE Access*, vol. 8, pp. 188284–188298, 2020.

[13] T. Kim, P. Bhargava, C. V. Poulton, J. Notaros, A. Yaacobi, E. Timurdogan, C. Baiocco, N. Fahrenkopf, S. Kruger, T. Ngai, Y. Timalsina, M. R. Watts, and V. Stojanović, "A single-chip optical phased array in a wafer-scale silicon photonics/cmos 3d-integration platform," *IEEE Journal of Solid-State Circuits*, vol. 54, no. 11, pp. 3061–3074, 2019.

[14] Y. Shuai, Z. Zhou, and H. Su, "Toward practical optical phased arrays through grating antenna engineering," *Photonics*, vol. 10, no. 5, 2023.

[15] C. A. Balanis, *Antenna theory: Analysis and Design*. Hoboken, N.J: John Wiley & Sons, Inc., 4. ed ed., 2016.

[16] W. Tong, E. Yang, Y. Pang, H. Yang, X. Qian, R. Yang, B. Hu, J. Dong, and X. Zhang, "An efficient, fast-responding, low-loss thermo-optic phase shifter based on a hydrogen-doped indium oxide microheater," *Laser & Photonics Reviews*, vol. 17, no. 9, p. 2201032, 2023.

[17] Y. Zhang, Y.-C. Ling, K. Zhang, C. Gentry, D. Sadighi, G. Whaley, J. Colosimo, P. Suni, and S. J. B. Yoo, "Sub-wavelength-pitch silicon-photonic optical phased array for large field-of-regard coherent optical beam steering," *Opt. Express*, vol. 27, pp. 1929–1940, Feb 2019.

[18] T. Komljenovic, R. Helkey, L. Coldren, and J. E. Bowers, "Sparse aperiodic arrays for optical beam forming and lidar," *Opt. Express*, vol. 25, pp. 2511–2528, Feb 2017.

[19] C. Bencivenni, *Aperiodic Array Synthesis for Telecommunications*. PhD thesis, 05 2017.

[20] "Ieee standard for definitions of terms for antennas," *IEEE Std 145-2013 (Revision of IEEE Std 145-1993)*, pp. 1–50, 2014.

[21] T. Dong, J. He, X. He, Y. Xu, and J. Zhou, "Hybrid design approach of optical phased array with wide beam steering range and low side-lobe level," *Opt. Lett.*, vol. 47, pp. 806–809, Feb 2022.

[22] Z. Wang, P. Ma, Y. Yang, L. Cui, L. Yu, G. Luo, P. Wang, J. Pan, Y. Su, and Y. Zhang, "Non-uniform optical phased array with a large steering angle and high side mode suppression ratio," *Appl. Opt.*, vol. 61, pp. 10788–10793, Dec 2022.

[23] C. Liu, W. Xu, L. Zhou, L. Lu, and J. Chen, "Multi-agent genetic algorithm for sparse optical phased array optimization," in *2019 Asia Communications and Photonics Conference (ACP)*, pp. 1–3, 2019.

[24] K. Du, R. Wang, J. Guo, R. Jiang, D. Kan, and Y. Zhang, "Design of a sparse array for a one-dimensional non-uniform optical phased array," *J. Opt. Soc. Am. B*, vol. 39, pp. 1141–1146, Apr 2022.

[25] X. He, T. Dong, J. He, and Y. Xu, "A design approach of optical phased array with low side lobe level and wide angle steering range," *Photonics*, vol. 8, no. 3, 2021.

[26] X. Zhao, Q. Yang, and Y. Zhang, "Compressed sensing approach for pattern synthesis of maximally sparse non-uniform linear array," *IET Microwaves, Antennas & Propagation*, vol. 8, no. 5, pp. 301–307, 2014.

[27] M. B. Hawes and W. Liu, "Robust sparse antenna array design via compressive sensing," in *2013 18th International Conference on Digital Signal Processing (DSP)*, pp. 1–5, 2013.

[28] D. Pinchera, M. D. Migliore, F. Schettino, M. Lucido, and G. Panariello, "An effective compressed-sensing inspired deterministic algorithm for sparse array synthesis," *IEEE Transactions on Antennas and Propagation*, vol. 66, no. 1, pp. 149–159, 2018.

[29] B. K. Natarajan, "Sparse approximate solutions to linear systems," *SIAM Journal on Computing*, vol. 24, no. 2, pp. 227–234, 1995.

[30] R. Tibshirani, "Regression shrinkage and selection via the lasso," *Journal of the Royal Statistical Society. Series B (Methodological)*, vol. 58, no. 1, pp. 267–288, 1996.

[31] M. Grant and S. Boyd, "CVX: Matlab software for disciplined convex programming, version 2.1." http://cvxr.com/cvx, Mar. 2014.

[32] M. Grant and S. Boyd, "Graph implementations for nonsmooth convex programs," in *Recent Advances in Learning and Control* (V. Blondel, S. Boyd, and H. Kimura, eds.), Lecture Notes in Control and Information Sciences, pp. 95–110, Springer-Verlag Limited, 2008. http://stanford.edu/~boyd/graph_dcp.html.

[33] S. Yang, B. Liu, Z. Hong, and Z. Zhang, "Low-complexity sparse array synthesis based on off-grid compressive sensing," *IEEE Antennas and Wireless Propagation Letters*, vol. 21, no. 12, pp. 2322–2326, 2022.

[34] S. Joshi and S. Boyd, "Sensor selection via convex optimization," *IEEE Transactions on Signal Processing*, vol. 57, no. 2, pp. 451–462, 2009.

[35] V. Roy, S. P. Chepuri, and G. Leus, "Sparsity-enforcing sensor selection for doa estimation," in *2013 5th IEEE International Workshop on Computational Advances in Multi-Sensor Adaptive Processing (CAMSAP)*, pp. 340–343, 2013.

[36] P. Stoica, H. He, and J. Li, "New algorithms for designing unimodular sequences with good correlation properties," *IEEE Transactions on Signal Processing*, vol. 57, no. 4, pp. 1415–1425, 2009.

[37] W. Fan, J. Liang, X. Fan, and H. C. So, "A unified sparse array design framework for beampattern synthesis," *Signal Processing*, vol. 182, p. 107930, 2021.

[38] G. Tang, B. N. Bhaskar, P. Shah, and B. Recht, "Compressed sensing off the grid," *IEEE Transactions on Information Theory*, vol. 59, no. 11, pp. 7465–7490, 2013.

[39] Z. Wang, G. Sun, J. Tong, and Y. Ji, "Pattern synthesis for sparse linear arrays via atomic norm minimization," *IEEE Antennas and Wireless Propagation Letters*, vol. 20, no. 12, pp. 2215–2219, 2021.